AD________________

Award Number: DAMD17-01-1-0330

TITLE: Image-Guided Surgery of Primary Breast Cancer Using Ultrasound Phased Arrays

PRINCIPAL INVESTIGATOR: Emad S. Ebbini, Ph.D.

CONTRACTING ORGANIZATION: University of Minnesota
Minneapolis, Minnesota 55455-2070

REPORT DATE: July 2003

TYPE OF REPORT: Annual

PREPARED FOR: U.S. Army Medical Research and Materiel Command
Fort Detrick, Maryland 21702-5012

DISTRIBUTION STATEMENT: Approved for Public Release;
Distribution Unlimited

REPORT DOCUMENTATION PAGE

Form Approved
OMB No. 074-0188

1. AGENCY USE ONLY (Leave blank)

2. REPORT DATE
July 2003

3. REPORT TYPE AND DATES COVERED
Annual (1 Jul 2002-30 Jun 2003)

4. TITLE AND SUBTITLE
Image-Guided Surgery of Primary Breast Cancer Using Ultrasound Phased Arrays

5. FUNDING NUMBERS
DAMD17-01-1-0330

6. AUTHOR(S)
Emad S. Ebbini, Ph.D.

7. PERFORMING ORGANIZATION NAME(S) AND ADDRESS(ES)
University of Minnesota
Minneapolis, Minnesota 55455-2070

E-Mail: emad@ece.umn.edu

8. PERFORMING ORGANIZATION REPORT NUMBER

9. SPONSORING / MONITORING AGENCY NAME(S) AND ADDRESS(ES)
U.S. Army Medical Research and Materiel Command
Fort Detrick, Maryland 21702-5012

10. SPONSORING / MONITORING AGENCY REPORT NUMBER

11. SUPPLEMENTARY NOTES

12a. DISTRIBUTION / AVAILABILITY STATEMENT
Approved for Public Release; Distribution Unlimited

12b. DISTRIBUTION CODE

13. ABSTRACT (Maximum 200 Words)

Recent developments of piezocomposite transducer technology have lead to the development of new generation of ultrasound phased arrays with imaging and therapeutic capabilities. These dual-mode arrays provide an ideal nonionizing noninvasive tool for the treatment of primary breast cancer. This project investigates the thresholds for tissue damage under a variety of exposure conditions to high-intensity focused ultrasound from dual-mode arrays. In addition, we investigate new imaging techniques for enhanced visualization of thermal lesions in tissue media. These investigations are carried on *ex-vivo* animal tissue and *in-vitro* breast tissue and will lead to the design of a new generation of phased array drivers capable of supporting both the imaging and therapeutic requirements of the dual-mode system. During the second year of the grant, we have focused on the complete characterization of the imaging capabilities of the dual-mode array prototype for visualization of lesions in *ex vivo* tissue. We have also compared these imaging results with those obtained using a commercially available diagnostic scanner. The results validated the dual-more array approach and allowed us to finalize the design of the real-time data collection and beamforming algorithm. We are on track towards implementing a real-time dual-mode system suitable for *in vivo* animal experiments.

14. SUBJECT TERMS
Thermal ablation; Ultrasound Imaging; Noninvasive Surgery

15. NUMBER OF PAGES
48

16. PRICE CODE

17. SECURITY CLASSIFICATION OF REPORT
Unclassified

18. SECURITY CLASSIFICATION OF THIS PAGE
Unclassified

19. SECURITY CLASSIFICATION OF ABSTRACT
Unclassified

20. LIMITATION OF ABSTRACT
Unlimited

NSN 7540-01-280-5500

Standard Form 298 (Rev. 2-89)
Prescribed by ANSI Std. Z39-18
298-102

Table of Contents

Introduction

High-intensity focused ultrasound (HIFU) is gaining wider acceptance in noninvasive or minimally invasive targeting of abnormal tissues (e.g. cancer) for destruction. Piezocomposite transducer technology, especially for phased arrays, is providing high-quality HIFU applicators with increased bandwidth and reduced parasitic cross coupling between the array elements. In addition to increasing the efficacy of HIFU applicators, these technological enhancements allow for the use of HIFU arrays in imaging the target region before, after, and intermittently during lesion formation. This leads to a unique paradigm of image-guided surgery with HIFU in which the coordinate systems for both therapy and imaging are inherently registered. This project investigates the feasibility of using piezocomposite phased arrays as dual-mode applicators for the noninvasive treatment of primary breast cancers. Both therapeutic and imaging capabilities of the dual-mode arrays are investigated leading to a real-time dual-mode array system to be used in pursuing *in vivo* animal experiments in the future.

Body

This report is structured in accordance with the approved statement of work (SoW). In what follows, we give the tasks and subtasks of the approved SoW with each subtask followed directly by what has been accomplished with respect to it in year 2. For the subtasks planned for years 1 and 3 of the grant period, they are given here for completeness, with short comments indicating their status, e.g. subtasks completed in year 1 as indicated in year 1 progress report.

Task 1. Thresholds for Thermal Ablation of Breast and Fatty Tissue (Months 1 – 12):

a) *Investigation of the intensity/exposure threshold curve; lesion size and characterization of damage (1 – 3):* Completed (Year 1 Report)
b) *Imaging of discrete thermal lesions with therapeutic arrays (1 – 3):* Completed (Year 1 Report).
c) *Long-duration volumetric ablation of porcine fatty tissue (3 – 9):* Completed (Year 1 Report).
d) *Imaging of volumetric ablations using the therapeutic array and diagnostic scanners (3 – 12):* Completed (Appendix IV).

Task 2. Treatment Planning and Optimization of Volumetric Ablation with Phased Arrays in Fatty Tissue (Months 6 – 24):

a) *Thermal modeling based on bioheat equation and Saparato and Dewey thermal dose integral for damage: Discrete lesions (6 – 12):* Completed (Year 1 Report)
b) *Thermal modeling for multiple lesions with variable levels of proximity and cooling time between shots (12 – 18):* We have simulated several treatment scenarios feasible with the dual mode arrays. Starting with the conventional procedure of forming a volumetric lesion by doing a series of discrete lesions one at a time with sufficient wait time between lesions to allow for the temperature to cool down (close to base line). This technique requires long waiting time between (thus leading to elongating the overall treatment time) if one is to avoid excessive heating in the prefocal region, which could lead to unintended damage of intervening tissue. We have also investigated the newly emerging technique of (electronically) raster scanning the therapeutic beam continuously at speeds of 1 – 3 mm/s to form volumetric lesion.

While the origin of this technique was proposed by Dr. ter Haar and first used clinically on the Chongqing HIFU system, it was very nicely illustrated *in vitro* by the group at the University of Washington in their recent presentations. We have also carried out some tissue heating experiments performing the raster scan approach to confirm the simulation results. The results confirm that the raster scan approach is superior to the shoot-and-wait approach in terms of treatment time and prefocal heating.

c) *Optimization of multiple-focus phased array patterns for simultaneous placement multiple discrete lesions (12 – 24):* We have also begun investigating the use of multiple focus patterns for the minimization of collateral damage in the prefocal region. This follows work done much earlier by the PI in investigating phased arrays for hyperthermia [Ebbini:91]. For the 64-element prototype used in this investigation, multiple-focus patterns do not give a distinct advantage over the raster scan method described in the previous subtask. This is not surprising given the relatively small number of array elements allowing for only a small number of simultaneous foci (2 4). Simulations of other 2D arrays with larger number of elements, however, continue to show that multiple-focus patterns offer significant advantage in reducing prefocal heating compared with any form of mechanical scanning (including the raster scan method).

Task 3. Detection and Localization of Cavitation Activity During Thermal Lesion Formation in Breast and Fatty Tissue (Months 1 – 24):

a) *Detection of subharmonic activity in single-channel and beamformed data (1 – 12):* Completed (Year 1 Report).

b) *Localization of cavitation from beamforming of multiple receiving channels (12 – 24):* We are still unable to demonstrate the sensitivity of the array elements to subharmonic generation using short (microsecond) imaging pulses suitable for localization. However, we still think that localization of cavitation events using microsecond pulses is feasible. We intend to order custom designed transducers, similar to the prototype we already have, with sufficient number of hydrophones integrated with the transducer. The new design will attempt to improve the isolation between the therapeutic array elements and the receiving hydrophones (so they can be used simultaneously with the therapeutic excitation). Furthermore, the hydrophones will be designed to have maximum sensitivity at the subharmonic. The use of an array of receiving hydrophones (on the order of 8 elements) will still allow us to achieve localization (provided that we can consistently produce cavitational oscillations with microsecond excitation pulses).

c) *Localization using time-frequency and related methods (6 – 18):* Our intuition with regard to the harmonic content of echoes from HIFU-induced thermal lesions is supported by data from numerous lesion formation experiments. We have believed all along that HIFU beams produce gas bubbles in the target tissue within the beam waist in the focal region. At normal exposure, these are stable microbubbles that can be beneficial in enhancing the power deposition at the target. They are also responsible for significant increase in echogenecity and second harmonic generation, especially when imaged at the therapeutic frequency. The figure below shows 25 dB grayscale images of *ex vivo* liver tissue before and after lesion formation using a 3 second exposure at 850 W/cm^2. One can see the increase in echogenecity at the lesion location (92 102 mm axial). On the right hand side, spectrograms from the RF line passing through the lesion (indicated by the arrows) are computed with 60 dB dynamic range. The spectrogram produced from the image after lesion formation shows high level of second harmonic activity localized to the lesion boundaries. It is this kind of observation that led to the development of the second harmonic imaging and, subsequently, to the quadratic imaging using the second order Volterra filters.

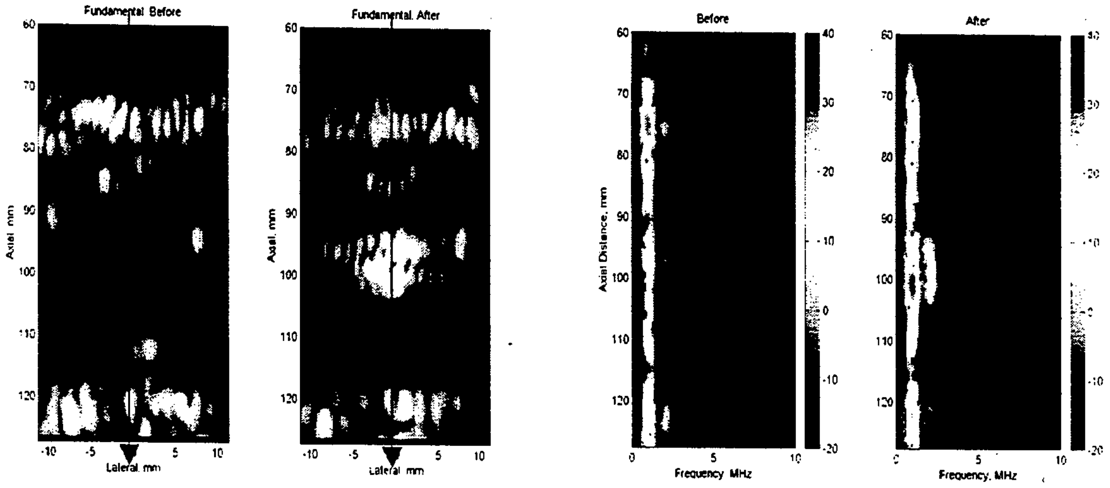

Task 4. Image Characterization of Thermal Lesions in Breast and Fatty Tissue (Months 1 – 24)

a) *Characterization of grayscale images for discrete thermal lesions (1 – 6):* Completed (Year 1 Report).
b) *Characterization of tissue dependent parameters (1 – 12):* Completed (Year 1 Report: (Expected) negative results).
c) *Characterization of second harmonic imaging (12 – 24):* Over the past 18 months, we have focused our attention on quadratic imaging which results from the second order Volterra filter formulation. The application of this filter to the lesion visualization is described in Appendix II and Appendix IV for image data acquired with a commercial diagnostic system. Appendix III describe its application to image data acquired with the dual-mode array. A fuller description is provided in the patent application and the journal paper. The basic idea behind quadratic filtering is illustrated by the figure below whereby the beamformed RF data from the array, $y(n)$, is decomposed into a linear and quadratic components as shown. We have developed an algorithm for deriving the linear and quadratic filters, h_L and h_Q, shown in the figure.

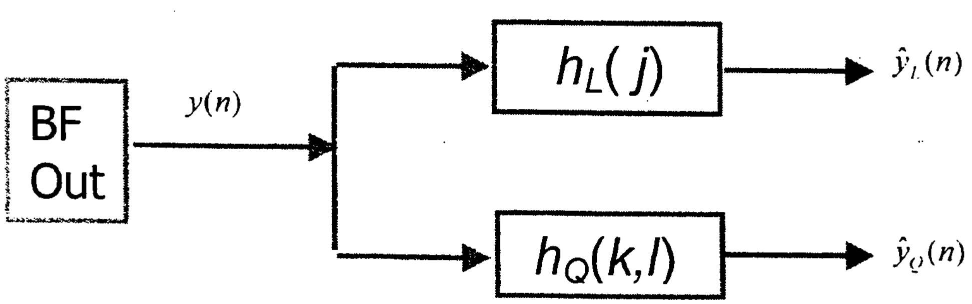

d) *Correlation of imaging parameters with histologic characterization of tissue ablations (12 - 24):* This is currently ongoing work. We have requested the addition of Dr. Robert Griffin from the Department of Therapeutic Radiology as an investigator on this project to help with this task beginning the 3rd year of the project. We have not yet heard from the program manager with regards to this request.

Task 5. Image-based Adaptive Refocusing of Therapeutic Arrays in Inhomogeneous Fatty Tissue (Months 12 - 24)

Focusing with reference to natural specular targets (12 – 18): The idea behind this task may be illustrated easily by Figure 1, which shows grayscale (25 dB) images of a fresh (untreated) sample of porcine liver. The image on the left hand side was acquired using single-transmit focus at the geometric center. Two large reflectors (blood vessels) and two smaller ones can be seen in the image. Using this image, the coordinates of the reflector at (5,90) mm were obtained. This was done through an interface program running under MATLAB whereby the user clicks the mouse on a target point in the image and the program finds the coordinates of the target based on the beamforming data that produced the image in the first place. We have then used the coordinates of the target to compute the delays needed to focus the transmit beam on this target. These delays were then used to produce the single transmit beam needed to obtain the image on the right hand side (25 dB dynamic range). The image clearly shows that the target is illuminated while the other three vessels are relatively dim, especially the vessel at (-5,90+). This result is quite significant as it shows that:

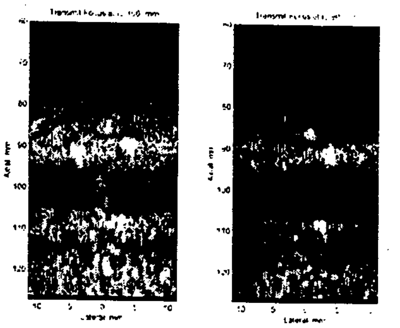

Figure 1 The image to the left is obtained using a single transmit focus along the central axis. The image to the right is obtained by a single transmit focus at the blood vessel at 90 mm axial and 5 mm lateral.

1. Critical structures (e.g., significant blood vessels) in the vicinity of the focus point of the transmit focus are illuminated by its sidelobe and can be seen in the single-transmit imaging mode.
2. Spatial coordinates of these critical structures can be accurately estimated from the beamformed single-transmit images.
3. Based on their estimated coordinates, these critical structures can be targeted (or avoided) by synthesizing transmit beams with maxima (or nulls) at these points.

Figure 1 shows the case of targeting a blood vessel with the transmit beam. One could have just as easily generated a beam that generates a minimum at the vessel location (avoidance). Many other scenarios can be envisioned once this capability is developed for guidance.

Temperature feedback (12 – 24): The sensitivity of the speckle component of the dual-mode array to temperature changes has been established experimentally. We have developed two different temperature imaging algorithms (based on pulse-echo ultrasound) under previous NIH funding (Seip and Ebbini and Simon and Ebbini). We fully expect that temperature feedback will be implemented with the dual-mode array system.

Discrete thermal lesions as beacons (12 – 24): This works in a similar manner to the illustration in Figure 1. However, it will not work with extended lesions. Our original plan was to generate a very small lesion that appears as a point reflector in the image and use it as a reference point. Our results so far provide a proof of concept. It is expected that the actual implementation of this procedure will be tied closely to establishing the thresholds for damage in the target tissue, e.g. breast tissue.

Task 6. Real-time Dual-mode Phased Array System for Volumetric Thermal Ablation of Breast and Fatty Tissue (Months 1 – 36)

a) Design and fabrication of 64-channel receive system (1 – 12): A new receiver circuit employing multiplexers for minimizing the number of analog-to-digital (A/D) converters has been designed and fabricated. This will significantly reduce the cost and complexity of the receive electronics. High-speed multiplexers allowed us to perform 8:1 or 4:1 multiplexing to each A/D while maintaining a minimum sampling rate of 10 MHz. This is sufficient for the dual-mode array operating at 1 MHz (and can capture the second harmonic without aliasing). Results from this new circuit will be reported at the Ultrasonics Symposium in October.

b) Design and fabrication of transmit/receive control circuitry (1 – 18): Completed (Year 1 Report).

c) DSP-based real-time beamformer (12 – 30): We have identified a VXI based real-time controller for beamforming. This controller will be sufficiently fast to perform real-time beamforming and uploading of image data to the controller workstation.

d) Experimental testing, calibration, and characterization of imaging system (24 - 36): We are on track for testing and characterization of the system for real-time data acquisition from all channels during the first half of the third year. We expect to be able to form images with a frame rate on the order of 10 – 15 frame per second. If this is achieved, we will be in an excellent shape to propose the use of the dual-mode system *in vivo* animal experiments as part of a future grant (possibly from the NIH).

Key Research Accomplishments

- We have established that the real-time harmonic activity during and after lesion formation is observable using diagnostic scanners (Technos MPX, Esaote, S.p.A., Genoa Italy). Hypothesis on microbubble activity is strengthened by real-time imaging results using the pulse inversion technique (Appendix II).
- We have extended the second harmonic imaging results to quadratic imaging using the second-order Volterra filter. This nonlinear imaging mode is superior to second harmonic imaging in that it improves spatial and contrast resolution and virtually eliminates beamforming artifacts. The latter severely limits the dynamic range of the 2nd harmonic imaging technique in single-transmit imaging mode. (Appendix II, III, IV).
- We have established the correlation between pulse inversion data and quadratic data for discrete lesions (Appendix II) and volumetric lesions (Appendix IV).
- We have demonstrated that nonlinear imaging methods like pulse inversion and quadratic filtering produce more accurate maps of the actual lesions (Appendix IV).
- Full characterization of the imaging capabilities of our 64-element prototype dual-mode array. Comparison with diagnostic imaging using the Esaote Technos MPX scanner (CA421 convex for abdominal imaging). This will be reported at the 2003 International Ultrasonics Symposium in October.
- Characterization of the transient behavior of the harmonic contents of the echo signal from the lesion location in *ex vivo* tissue (several different tissues used). This will be reported at the 2003 International Ultrasonics Symposium in October.

Reportable Outcomes

Steidl, C.; Hui Yao; Phukpattaranont, P.; Ebbini, E.S., "Dual-mode ultrasound phased arrays for noninvasive surgery: post-beamforming image compounding algorithms for enhanced visualization of thermal lesions," Biomedical Imaging, 2002. Proceedings. 2002 IEEE International Symposium on , 7-10 July 2002, Page(s): 429 -432.

Hui Yao; Phukpattaranont, P.; Ebbini, E.S.,"Nonlinear methods for visualization of HIFU-induced lesions," Proceedings of the 2nd International Symposium on Therapeutic Ultrasound (ISTU2), 29 July - 1 August, Seattle, WA, Editors: Andrew, Crum, and Vaezy, 2002, Page(s): 282 - 289.

Hui Yao; Phukpattaranont, P.; Ebbini, E.S., "Detection and mapping of thermal lesions using dual-mode ultrasound phased arrays," Proceedings of the 2002 IEEE Ultrasonics Symposium, Volume: 2, Oct 8-11, 2002, Page(s): 1435 -1438.

Hui Yao; Phukpattaranont, P.; Ebbini, E.S.,"Nonlinear imaging methods for characterization of HIFU-induced lesions," Proceedings of the SPIE vol. 4954, Thermal Treatment of Tissue: Energy Delivery and Assessment II, Editor: T.P. Ryan, 2003, Page(s): 183 - 191.

Emad S. Ebbini, "Nonlinear pulse-echo imaging methods for HIFU-induced lesion visualization," 145th Meeting of the Acoustical Society of America, JASA, vol. 113, no. 4, 2003, Page: 2309 (*Invited*).

Emad S. Ebbini, "Dual-mode HIFU arrays," 3rd International Symposium on Therapeutic Ultrasound (ISTU3), Lyon, France 22 - 25 June, 2003, manuscript in preparation.

Emad S. Ebbini and Pornchai Phukpattaranont, "Ultrasound imaging system and method using non-linear post-beamforming filter," Patent application to the US Patent and Trademark Office (Initial application 10 May, 2002; Continuation-in-part 9 May 2003).

Pornchai Phukpattaranont and Emad S. Ebbini, "Post-beamforming second-order Volterra filter for pulse-echo ultrasonic imaging", *IEEE Trans. on Ultrasonics, Ferroelectrics and Frequency Control, August 2003.*

Conclusions

Our efforts during the second year of the grant were focused on validating and characterizing the imaging capabilities of the 64-element dual-mode array prototype. In addition, we have generalized the harmonic processing of the echo signal to quadratic processing. This approach was shown to be superior in terms of enhancing the spatial and contrast resolution of lesion images. Quadratic imaging was also shown to produce results comparable to pulse inversion imaging, an imaging method designed to detect microbubble activity (contrast-agent imaging). Compared to pulse inversion, quadratic imaging is not sensitive to motion and has wider dynamic range.

Our characterization of the 64-element dual-mode array prototype is as follows:

Therapeutic performance: Free field focal intensities up to 3500 W/cm^2 in a region approximately 4 cm in diameter around the geometric focus (with electronic scanning).

Imaging Performance: Axial resolution of 3 mm, lateral resolution of 1.1 mm. This is opposite to typical diagnostic systems, which have better axial resolution (< 1 mm) than axial resolution (~2 mm). This is due to the relatively narrow bandwidth (leading to reduced axial resolution) and the large aperture (leading to excellent lateral resolution) of the dual-mode array prototype. Furthermore, we have shown that the dynamic range of 50 dB in an elliptical region around the geometric center (major diameter 6 cm and minor diameter of 5 cm). High contrast targets like large blood vessels are always visible. Speckle contrast targets smaller than 4 mm are indistinguishable from a point specular reflector.

What does this mean? Our dual mode approach is a viable approach for image guidance as we can recognize structures and markers in the target region. We have also established unequivocally that lesions can be mapped accurately based on changes in their echogenecity during and immediately after formation. This remains one of the most attractive features of our approach, especially when single-transmit focusing is used. This mode is unique because it allows us to inspect the changes in the echoes precisely at the expected lesion location (since the imaging transmit beam is obtained from the therapeutic beam itself). It also allows for the detection of any critical structures in the path of the therapeutic beam. Therefore, imaging with the therapeutic beam before lesion formation is probably the most powerful tool for avoiding collateral damage upon targeting specific tissue for damage.

References

[Ebbini:91] E. Ebbini and C. Cain, "A spherical-section ultrasound phased array applicator for deep localized hyperthermia," *IEEE Trans. Biomed. Eng.*, vol. 38, pp. 634-643, 1991.

[Seip:95a] R. Seip and E. Ebbini, "Non-invasive estimation of tissue temperature response to heating fields using diagnostic ultrasound," *IEEE Trans. Biomed. Eng.*, vol. 42, no. 8, pp. 828-839, August 1995.

[Seip:95b] R. Seip, P. VanBaren, C. Simon, and E. Ebbini, "Non-invasive spatio-temporal temperature change estimation using diagnostic ultrasound," in *IEEE Ultrason. Symp.*, pp.1613-1616, November 1995.

[Seip:96a] R. Seip, *Feedback for Ultrasound Thermotherapy*, PhD thesis, EECS, University of Michigan, February 1996.

[Seip:96b] R. Seip, P. VanBaren, C. Cain, and E. Ebbini, "Non-invasive real-time multipoint temperature control for ultrasound phased array treatments," *IEEE Trans. Ultrason., Ferroelec., Freq. Contr.*, vol. 43, no. 6, pp.1063-1073, November 1996.

[Simon:98c] C. Simon, P. VanBaren, and E. Ebbini, "Two-dimensional temperature estimation using diagnostic ultrasound," *IEEE Trans. Ultrason. Ferroelec., Freq. Contr.*, vol. 45, no. 4, pp. 1088-1099, July 1998.

Appendices

I. *Steidl, C.; Hui Yao; Phukpattaranont, P.; Ebbini, E.S.,* "Dual-mode ultrasound phased arrays for noninvasive surgery: post-beamforming image compounding algorithms for enhanced visualization of thermal lesions," Biomedical Imaging, 2002. Proceedings. 2002 IEEE International Symposium on , 7-10 July 2002, Page(s): 429 -432.

II. *Hui Yao; Phukpattaranont, P.; Ebbini, E.S.,* "Nonlinear methods for visualization of HIFU-induced lesions," Proceedings of the 2nd International Symposium on Therapeutic Ultrasound (ISTU2), 29 July - 1 August, Seattle, WA, Editors: Andrew, Crum, and Vaezy, 2002, Page(s): 282 - 289.

III. *Hui Yao; Phukpattaranont, P.; Ebbini, E.S.,* "Detection and mapping of thermal lesions using dual-mode ultrasound phased arrays," Proceedings of the 2002 IEEE Ultrasonics Symposium, Volume: 2, Oct 8-11, 2002, Page(s): 1435 -1438.

IV. *Hui Yao; Phukpattaranont, P.; Ebbini, E.S.,* "Nonlinear imaging methods for characterization of HIFU-induced lesions," Proceedings of the SPIE vol. 4954, Thermal Treatment of Tissue: Energy Delivery and Assessment II, Editor: T.P. Ryan, 2003, Page(s): 183 - 191.

V. *Pornchai Phukpattaranont and Emad S. Ebbini*, "Post-beamforming second-order Volterra filter for pulse-echo ultrasonic imaging", *IEEE Trans. on Ultrasonics, Ferroelectrics and Frequency Control, August 2003.*

Appendix 1

DUAL-MODE ULTRASOUND PHASED ARRAYS FOR NONINVASIVE SURGERY: POST-BEAMFORMING IMAGE COMPOUNDING ALGORITHMS FOR ENHANCED VISUALIZATION OF THERMAL LESIONS

Charles Steidl, Hui Yao, Pornchai Phukpattaranont and Emad S. Ebbini

Department of Electrical and Computer Engineering
University of Minnesota
Minneapolis, MN 55455

Abstract- **A post-beamforming nonlinear compounding algorithm for ultrasonic imaging is presented. Fundamental and harmonic image components from beamfromed radio frequency (RF) data are extracted, envelope detected and compounded using a spatial compounding functions (SCFs) derived from the transmit/receive beamforming topology used in obtaining the RF data. This is specially useful for applications where single-transmit focus (STF) imaging is used. In this paper, we present results from STF imaging experiments using a novel dual-mode phased array system for image-guided surgery. In particular, we address the enhancement of the echogenicity of thermal lesions formed in *ex vivo* tissue. It is shown that new nonlinear image compounding algorithm produces 25 - 30 dB enhancement in lesion echogenicity without loss in spatial resolution. This is to be compared with a typical enhancement of 5 dB achieved by standard echographic imaging and 20 dB achieved by second harmonic imaging alone. In addition, images resulting from the new algorithm are virtually free of beamforming artifacts that can severely degrade the performance of 2nd harmonic imaging.**

1. INTRODUCTION

Image guidance has long been recognized as the "enabling technology" for noninvasive thermal surgery. Highly refined energy application devices have been developed and for years. However, without reliable imaging techniques for visualization of thermal lesions, noninvasive thermal surgery has failed to find widespread acceptance in the clinic. Recently, image guidance methods based on well established imaging modalities like MRI[3], CT[5], or ultrasound [4, 8] have been proposed. Other imaging modalities are also being developed and may become available in the foreseeable future[6, 7].

An area unique to ultrasound that could revolutionize the field of image-guided surgery is the development of a new generation of dual-mode high-power phased array systems capable of both imaging and therapy [8, 9]. These piezocomposite transducers can produce focal intensity levels needed for ablative and coagulative thermal surgery with high precision. Furthermore, the operating bandwidth of such transducers allows for imaging the treatment region with adequate image quality to delineate important landmarks within and around the target volume. With these capabilities, it is possible to operate these arrays in a "self-registration" mode whereby the imaging capabilities of the array are utilized in characterization of the tissue response precisely at the expected lesion location. This is due to the fact that the beamforming is common to both the imaging and therapy modes. The main challenge to this approach is the low-contrast nature of speckle-ridden ultrasound images. This paper addresses a new post beamforming filter bank image reconstruction algorithm with nonlinear spatially weighted compounding algorithm to mitigate this problem. The design of this algorithm is motivated by the nonlinear nature of ultrasound propagation in tissue and the fact that thermal lesions are known to have increased level of harmonic generation. Experimental results demonstrate the potential of the new algorithm in both enhancing the lesion contrast and size/shape analysis.

2. IMAGE FORMATION MODEL

Figure 1 summarizes the image acquisition and image formation model. A 64-element array optimized for maximum energy delivery at 1 MHz operating frequency is used for lesion formation in sample tissue. Lesions are formed by focusing the array at a point within the target and maintaining high-power output for time intervals on the order of seconds (1 - 5 seconds typical). The power is interrupted for short intervals (milliseconds) to acquire image data by transmitting short (μs) pulses from all 64-elements and receiving on selected elements using a matrix switch. Once the image data set is collected, RF beamforming is performed to form standard echographic images of the target region.

Funded by Grant DAMD 17-01-1-330 from the US Army Medical Research and Materiel Command.

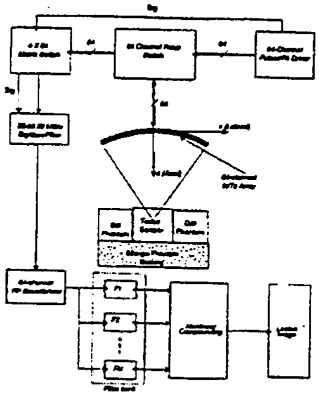

Fig. 1. Image Acquisition and Image Reconstruction Algorithm

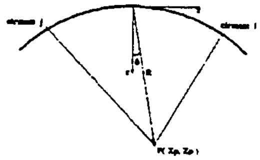

Fig. 2. Coordinate system used in the synthetic aperture imaging system.

2.1. Synthetic aperture imaging

Images are obtained using a full synthetic aperture technique [10]. The image pixel at coordinates (x_p, z_p) is therefore computed by (Fig. 2):

$$I(x_p, z_p) = \sum_{i=1}^{64} \sum_{j=1}^{64} A_i \cdot B_j \cdot s_{i,j}\left[(R_{ip} + R_{jp})/c\right], \quad (1)$$

where i is the transmit element index, j is the receive element index, A_i is the transmit apodization weight at element i, B_j is the receive apodization weight at element j, R_{ip} and R_{jp} are the distances from the transmit and receive elements, respectively, from the image pixel, c is the speed of sound in the medium being imaged, and $s_{i,j}(t)$ is the echo acquired when transmitting with element i and receiving with element j.

2.2. Single-Transmit Focus (STF) Imaging

The synthetic aperture imaging algorithm described above can be used to produce the highest quality conventional images that can be expected from a given array. However, due to the fact that transmit beams are synthesized by superposition of single-element transmit patterns, the nonlinear interactions of the real-time transmit beams cannot be accounted for using this imaging algorithm. Therefore, we have modified our 64-channel phased array driver to allow for pulsed transmission on all 64 channels simultaneously. This allowed us to use the full power of the transmit beams and, therefore, observe their nonlinear interactions with the tissue media. The image formation process due to a STF beam is a modified version of Equation (1) as follows:

$$I(x_p, z_p) = \sum_{j=1}^{64} B_j \cdot s_j\left[(R_0 + R_{jp})/c\right], \quad (2)$$

where $s_j(t)$ is the received waveform at element j due to the transmitted beam and R_0 is a fixed distance determined by the focal depth of the transmit beam. All other quantities in Equation (2) are the same as their counterparts in Equation (1). It should be noted that beamforming is performed in the RF domain using true delays, i.e., no baseband conversion is done. This retains all the frequency components in the beamformed data for postbeamforming filtering operations described below.

2.3. Post Beamforming Filtering

Since beamforming is performed in the RF domain, all the frequency components in the received echo signals are retained. This is important since the echo signals can be expected to contain a mix of harmonics (and possibly subharmonics) depending on the nonlinearity of the tissue medium being imaged. This is especially true for the STF imaging mode where the transmit power is sufficiently high to produce harmonic components in nonlinear tissue media. Postbeamforming filtering can be used to isolate specific harmonic components and/or enhance axial resolution if the SNR of the system is sufficiently high. Algorithms for postbeamforming filterbank image reconstruction for pulse-echo ultrasound can be found in [11]. For the purposes of this paper, the filter bank is formed of bandpass filters with center frequencies at a set of preselected harmonics (or subharmonics).

2.4. Nonlinear Compounding

Ultrasound propagation in tissue media is inherently nonlinear. RF echo signals obtained using modern scanners with wideband transducers carry harmonic components that are generated by the medium nonlinearity, i.e., they are not part of the originally transmitted imaging pulses. Since the tissue nonlinearity parameter exhibits higher contrast between various tissue compared to tissue reflectivity, imaging this parameter can lead to higher contrast images of soft tissue. For a variety of physical reasons, it is well known that thermal lesions generate higher harmonics at levels higher than normal tissues. By careful design of the transmit/receive beamforming and the post beamforming reconstructions filters, high contrast images of lesions can be formed from ultrasound images formed at the fundamental and some of its higher harmonics. In general, an optimal compounding rule must be derived based on statistical model of the imaged region and the expected lesion size/location. Furthermore, the quality of the beamforming at different harmonics or scales will be spatially heterogeneous. For example, since the array sampling function (in wavelengths) is coarser at the higher harmonics, images formed at these frequency will have high contrast along the axis of the transmit beam, but the contrast deteriorates quickly away from the main axis. Furthermore, since the harmonics are orders of magnitudes smaller than the fundamental, compounding is performed with log-compressed images after appropriate scaling. Therefore, with reference to Figure 1, the compounding is performed in two stages:

1. The outputs of the filterbank are envelope detected, scaled, and log compressed. The scaling of the individual harmonics can be derived from, for example, the specificity or contrast-to-tissue ratio (CTR):

   $$CTR = 10\log_{10}\left(\frac{\|\mathbf{y}_{C_i}\|_2^2}{\|\mathbf{y}_{T_i}\|_2^2}\right) \qquad (3)$$

   where $\|\mathbf{y}_{C_i}\|_2$ and $\|\mathbf{y}_{T_i}\|_2$ are the l_2 norms of the ith harmonic components from the contrast and normal tissue regions, respectively. These regions are easily identified under various imaging conditions. For instance, for the application described in this paper, the contrast region is the expected location of the thermal lesion (often visible on the standard echographic image).

2. A spatially-weighted sum of the harmonic components is performed. The weighting function is derived from the spatial contrast function (SCF) of the imaging array at the different harmonics.

Assuming that the envelope-detected, normalized and log-compressed images obtained from the filterbank are given by $I_1, I_2, \ldots, I_N$, then the compounded image is given by:

$$I(x,y) = \sum_{i=1}^{N} W_i S_i(x,y) I_i(x,y) \qquad (4)$$

where W_i is a weighting function reflecting the relative energy at the harmonic with respect to the fundamental at the (expected) lesion location and $S_i(x,y)$ is the SCF associated with the ith harmonic. This is can be obtained based on simulations of pulsed or CW calculations of the following ratio:

$$S_i(x,y) = \frac{\int_{ML} B_{r_i}(x,y;x')B_t(x,y_0;x')dx'}{\int_{SL} B_{r_i}(x,y;x')B_t(x,y_0;x')dx'}, \qquad (5)$$

where the subscripts $_{SL}$ and $_{ML}$ refer to sidelobe and mainlobe, respectively, and $B_{r_i}(x,y;x')$ is the ith harmonic (dynamic) receive focus at (x,y) and $B_t(x,y_0;x')$ is the transmit focus pattern (at the fundamental). Note that the SCF is a measure of the quality of the transmit/receive pattern at the ith harmonic. The higher the SCF the more confidence we have in the received data at the ith harmonic.

3. RESULTS

Figure 3 gives a typical result of a visualization experiment using the dual-mode array and the image compounding algorithm described above. The figure shows images obtained before and after lesion formation in an *ex-vivo* liver tissue samples. The expected lesions are cigar-shaped with length of 10 mm and width of 2 - 3 mm. All images are shown at 40 dB dynamic range and have the same axial and lateral extent. The lesion was formed at the geometric center of the array and was expected between 90 and 100 mm in the axial direction. All images show the front surface of the sample at 80 mm and the sponge backing phantom at 120 mm. Three pairs of images are shown, one before (left) and one after the lesion formation. The images on top of each figure are formed at the fundamental (1 MHz) while those at the center of each figure are formed at the 2nd harmonic (2 MHz). The pair at the bottom shows the compound image using Equation 4 and the SCFs shown in Figure 4. Each pair of images is displayed on a log scale and normalized such that the 0 dB corresponds to the maximum of the image on the RHS, i.e., the image of the target after lesion formation. While both the fundamental and harmonic images show enhanced lesion contrast, the harmonic images show a net increase in contrast by 22 dB along the direction of the transmit beam. On the other hand, the net increase in contrast at the fundamental is about 7 dB. In addition, the spatial definition of the lesion in the harmonic images is superior to the fundamental. However, while the harmonic images are superior both in terms of definition and contrast near the main axis of the transmit beam, the fundamental images better represent the tissue state off-axis. The compound images show a net increase in the lesion contrast on the order of 35 dB both axially and laterally. This result can be understood in light of a close examination of the SCRs shown in Figure 4. It is also interesting to note, however, that the compound image still shows major off-axis objects, e.g., blood vessel at axial distance of 110 mm and lateral distance of 5 mm. That is, the compounding algorithm removes the beamforming sidelobe artifacts, but not major scatterers in the vicinity of the transmit beam. This is one of the main objectives of STF imaging described in this paper.

4. CONCLUSIONS

We have shown that post beamforming filterbank reconstruction of ultrasound images at selected frequencies sensitive to harmonic generation in nonlinear media produces images appropriate for compounding. The results of applying the nonlinear compounding algorithm also demonstrate a significant increase in lesion contrast over enhancement

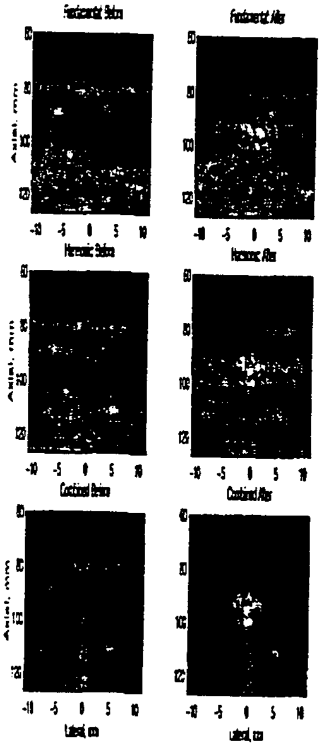

Fig. 3. Images before (left) and after lesion formation. All images are shown at 40 dB dynamic range.

achieved at either the fundamental or second harmonic. It is important to state that this contrast enhancement is achieved without loss in spatial resolution. This due to the fact that the bandpass filters used in separating the fundamental and harmonic components have wider bandwidth than the data bandwidth at these harmonics. The results shown in this paper suggest that dual-mode arrays with high contrast imaging capability suitable for real-time thermal lesion visualization are feasible. This leads to a most powerful paradigm for image guided surgery where the therapeutic and image-guidance coordinate systems are inherently registered.

5. REFERENCES

[1] B. Fallone, P. Moran, and E. Podgorsak, 'Noninvasive thermometry with a clinical X-ray scanner," *Med. Phys.*, vol. 9, no. 5, pp. 715–721, 1982.

[2] D. Parker, 'Applications of NMR imaging in hyperthermia: An evaluation of the potential for localized tissue heating and noninvasive temperature monitoring," *IEEE Trans. Biomed. Eng.*, vol. 31, no. 1, pp. 161–167, 1984.

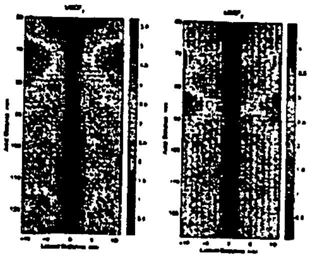

Fig. 4. Inverse of the SCRs for the fundamental (left) and the second harmonic. Transmit focus at 100 mm axial and 0 lateral.

[3] J. Poorter, C. Wagter, Y. Deene, C. Thomsen, F. Stahlberg, and E. Achten, 'Noninvasive MRI thermometry with the proton resonance frequency (PRF) method: In vivo results in human muscle," *Magn. Reson. Med.*, vol. 33, pp. 74–81, 1995.

[4] N. Sanghvi *et al.*, 'Noninvasive surgery of prostate tissue by high-intensity focused ultrasound," *IEEE Trans. UFFC*, vol. 43, no. 6, pp. 1099–1110, Nov. 1996.

[5] J. Jenne, M. Bahner, J. Spoo, P. Huber, R. Rastert, I. Simiantonakis, W. Lorenz, and J. Debus, 'CT on-line monitoring of HIFU therapy," *IEEE Ultrason. Symp.*, 1997.

[6] K.Paulsen, M.Moskowitz, T.Ryan, S.Mitchell, and P.Hoopes, 'Initial *in vivo* experience with EIT as a thermal estimator during hyperthermia," *Int. J. Hyperthermia*, vol. 12, no. 5, pp. 573–591, Sept. 1996.

[7] P.Meaney, K.Paulsen, A.Hartov, and R.Crane, 'Microwave imaging for tissue assessment: Initial evaluation in multitarget tissue-equivalent phantoms," *IEEE Trans. Biomed Eng.*, vol. 43, no. 9, pp. 878–890, Sept. 1996.

[8] E. Ebbini, P. VanBaren, and C. Simon, 'Image-guided noninvasive surgery with ultrasound phased arrays," *SPIE Bios: Surgical Applications of Energy*, 1998.

[9] C. Simon, J. Shen, T. Hall, and E. Ebbini, 'Combined ultrasound image guidance and therapy using a therapeutic phased array," *SPIE: Medical Imaging 1998*, vol. 3341, pp. San Diego, Feb. 1998.

[10] K. Thomenius, 'Evolution of ultrasound beamformers," *IEEE Ultrason. Symp.*, pp. 1615–1622, Nov. 1996.

[11] J. Shen and E. S. Ebbini, 'Filter-based coded-excitation system for high speed ultrasonic". *IEEE Trans. Medical Imaging*, 45(6), December 1998.

Appendix 2

Nonlinear Methods for Visualization of HIFU-Induced Lesions

Yao Hui, Pornchai Phukpattarnont and Emad S. Ebbini

Department of Electrical and Computer Engineering, University of Minnesota Twin Cities, Minneapolis, MN 55455

Abstract. Nonlinear ultrasonic imaging methods (like pulse inversion [1] and quadratic imaging based second-order Volterra filter [2]) are used in visualization of lesion formation in freshly excised tissue. Both of these methods are more sensitive to nonlinear echoes (e.g., due to micro-bubbles) than standard B-mode imaging. While all three methods typically show increased echogenicity at the lesion location, the nonlinear methods exhibit more localized echo enhancement than B-mode imaging. Therefore, nonlinear methods are better suited to lesion mapping for purposes of image guidance. Quadratic images have the added advantage of a significant increase in image dynamic range and noise reduction (a major limitation of pulse inversion imaging). The results shown in this report continue to support the hypothesis that micro-bubbles play an important role of lesion formation. Furthermore, the presence of microbubbles provides significant opportunity for mapping the treated tissue and potentially characterizing the nature of damage.

INTRODUCTION

We have used a dual-mode array described in [3] to form HIFU-induced thermal lesions in freshly excised degassed tissue under a variety of *normal exposure* and *over exposure conditions*. Single-transmit focus images were collected for over 100 lesions before and after lesion formation. These images have consistently shown 5 - 7 dB enhancement in the echogenicity from the lesion location in the standard echographic images. These results were much more consistent than the reported "flashes" on the B-scan images when diagnostic ultrasound systems are used to monitor HIFU lesion formation. Motivated by the excellent investigation by P. P. Lele reported in [4], we hypothesized that this change in echogenicity is due to stable microbubbles that can occur even at low insonation levels. Lele found that subharmonic emission due to microbubbles showed a monotonic increase with intensity from 150 mW/cm^2 to 1500 W/cm^2 without a distinct threshold for emission (measurements done *in vitro* and *in vivo* at 2.7 and 1.8 MHz). The consistency of the increase in echogenicity at the lesion may be explained by the fact that the microbubbles may already be resonant at the imaging frequency (same as the therapeutic HIFU beam when the dual-mode array is is used), perhaps a result of rectified diffusion.

The standard echographic images at the fundamental, however, offer limited contrast enhancement due to the speckle phenomenon. Therefore, they could not provide a reliable method for mapping the boundaries of HIFU-induced lesions. This lead us to try to exploit the nonlinear nature of the microbubbles to enhance the visualization and mapping of thermal lesions. The idea was that, if microbubbles are indeed present at the lesion location, they will generate nonlinear echoes that may be better suited for mapping. We have initially investigated second harmonic (SH) imaging as a means of enhancing the lesion contrast for improving the visualization of these images. SH images of thermal lesions have shown increase in the contrast on the order of 22 - 25 dB, but with decreased dynamic range of the resulting images [3]. A post-beamforming nonlinear compounding algorithm was shown to improve the contrast in lesion echogenicity to 30 - 35 dB without loss in dynamic range [5]. This was achieved by compounding the fundamental and the SH images using spatial compounding functions based on the receive beamforming characteristics of the dual-mode array at the fundamental and the SH frequencies. In this paper, we use a commercial imaging scanner with modifications to allow pulse inversion imaging in addition to standard B-mode imaging for the visualization of freshly excised tissue before, during, and after the formation of HIFU lesions.

NONLINEAR IMAGING METHODS

Pulse Inversion Imaging

This method was recently introduced by Burns and coworkers [6] for enhancing contrast echoes in contrast-assisted pulse-echo imaging. The basic implementation of this method entails the use of two pulses per image line. These pulses are carefully designed such that, $p_2(t) = -p_1(t - T_L)$, where T_L is some appropriate delay (on the order of the pulse-echo time from the maximum depth of interest). Summing the echoes resulting from the two pulses eliminates the odd-harmonic components from the echo signal (including the fundamental) while doubling the even-harmonic (mostly second) components. This method currently represents the leading approach for contrast-agent imaging, especially with low concentration and/or very low transmit signals to minimize the generation of tissue nonlinearity.

Quadratic Imaging Based On SVF

We have recently developed a new nonlinear imaging system based on the SVF [2]. This has a number of advantages when compared to PI imaging (e.g. requires only a single pulse per line and increased dynamic range).

Second-Order Volterra Model

Results from [2] have shown the validity of a second-order Volterra filer as a model for pulse-echo ultrasound imaging data from tissue mimicking media. In this section, the decomposition of received echo, i.e., output sequences only, into linear and quadratic components by using least-squares approach of second-order Volterra model will be considered and the detail of algorithm implementation to pulse-echo ultrasound imaging will be stated.

Signal Separation Model

The algorithm described in this section is adapted from [7]. The response of a quadratically nonlinear system, $y(n+1)$, can be predicted by a second-order Volterra model of past m values as follows:

$$\begin{aligned} y(n+1) &= y_L(n+1)+y_Q(n+1) \\ &= \sum_{i=0}^{m-1} y(n-i)h_L(i)+\sum_{j=0}^{m-1}\sum_{k=j}^{m-1} y(n-j)y(n-k)h_Q(j,k)+\varepsilon(n). \end{aligned} \tag{1}$$

where $h_L(i)$ is linear filter coefficients, $h_Q(j,k)$ represents quadratic filter coefficients and $\varepsilon(n)$ is a modelling error and/or a measurement noise which is assumed to be an independent, identically distributed(i.i.d) random variable with zero mean. That is, if the model coefficients are known, the echo signal can be decomposed into linear and quadratic components. The latter can be expected to better represent the quadratic response of the system than, say, the second harmonic component. The model coefficients can be obtained by setting the linear and quadratic prediction problem in Equation 1 to form a set of linear equations. Recognizing that the output is linear in terms of the (unknown) model coefficients, one obtains a matrix equation of the form:

$$\mathbf{f} = \mathbf{G}\mathbf{h} + \varepsilon. \tag{2}$$

where the vector $\mathbf{f}$, the matrix $\mathbf{G}$ and the error vector ε are

$$\begin{aligned} \mathbf{f} &= [y(n+1), y(n+2), \ldots, y(n+L)]^T \\ \mathbf{G} &= [\mathbf{y}(n), \mathbf{y}(n+1), \ldots, \mathbf{y}(n+L-1)]^T \\ \varepsilon &= [\varepsilon(n), \varepsilon(n+1), \ldots, \varepsilon(n+L-1)]^T. \end{aligned}$$

where the data vector, $\mathbf{y}$, is given by:

$$\begin{aligned} \mathbf{y}(n) = [&y(n), y(n-1), y(n-2), \ldots, y(n-m+1), \\ &y^2(n), y(n)y(n-1), \ldots, y^2(n-m+1)]^T \end{aligned}$$

and the filter coefficient vector, $\mathbf{h}$, is given by:

$$\begin{aligned} \mathbf{h} = [&h_L(0), h_L(1), h_L(2), \ldots, h_L(m-1), \\ &h_Q(0,0), h_Q(0,1), \ldots, h_Q(m-1, m-1)]^T. \end{aligned}$$

The details of the solution for the coefficients of the SVF model can be found in [8]. Briefly, a minimum-norm least-squares solution of (2) is obtained using *truncated singular value decomposition, TSVD*. To assess the performance of the signal separation model in enhancing the lesion visualization, we compute the contrast-to-tissue ratio:

$$CTR = 10\log_{10}\left(\frac{\|\mathbf{y}_{QC}\|_2^2}{\|\mathbf{y}_{QT}\|_2^2}\right) \tag{3}$$

where $\|y_{QC}\|_2$ and $\|y_{QT}\|_2$ are the l_2 norms of the quadratic components from the lesion and normal tissue regions, respectively. These regions are easily identified under various imaging conditions. For instance, for the application described in this paper, the contrast region is the expected location of the thermal lesion (often visible on the standard echographic image).

Implementation

The coefficients of the linear and quadratic components of the SVF model are obtained from the beamformed RF data. The implementation steps are as follows:

1. Using the standard echographic image, select a beamformed RF data segment from the expected lesion location.
2. Form the linear systems of equations according to (2).
3. Define contrast region (within the lesion) and normal tissue region for the computation of the mean-square error *MSE* and *CTR*.
4. Solve systems of linear equations by using TSVD regularization method.
5. Apply second-order Volterra filter to the beamformed RF data throughout the pulse-echo ultrasound image.
6. The quadratic component from the SVF can be displayed as a separate image or appropriately compounded with the linear component.

EXPERIMENTAL SETUP

Figure 1 shows a simple arrangement for the formation of HIFU lesions in freshly excised and degassed porcine livers samples. The therapy transducer is a 1.5 MHz single-element spherical-shell transducer with a radius of curvature equal to its diameter and equal to 63.5 mm (Etalon, Lizton, Indiana). The transducer is fixed to the back of a small tank as shown and driven by a power amplifier (ENI, Rochester, NY) and a programmable function generator. This assembly can be used in generating a variety of amplitude-modulated HIFU bursts from tens of milliseconds to several seconds long and intensities up to 3000 W/cm^2 (conservative estimate).

Real-time imaging is performed using a modified Technos MP system from ESAOTE, Genoa, Italy. The system is modified to allow imaging in pulse inversion mode in addition to normal B-mode imaging. In addition, a hardware module for capturing high-quality beamformed RF data allows us to capture and upload up to 60 seconds of full frame data with a specified frame rate. A CA 421 convex probe was used in acquiring image data for this paper. Image data was acquired in pulse inversion (PI) mode with a 2-cycle transmit pulse centered at 1.57 MHz. The imaging transducer was aligned so that the image plane is $x-z$ plane (to allow imaging the lesion along the axis of the therapy transducer.

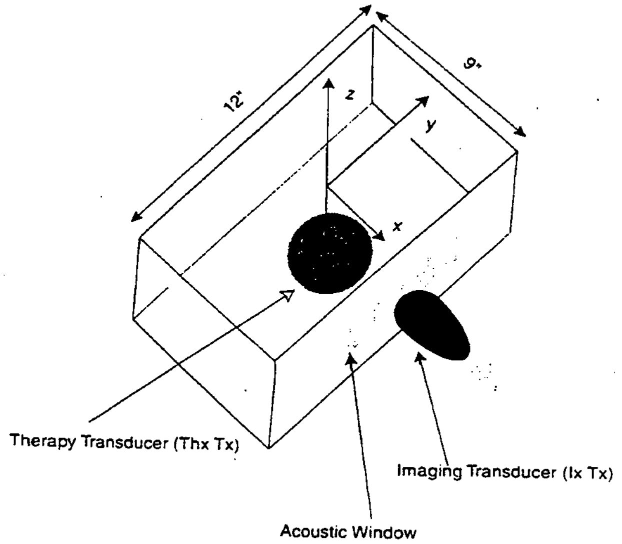

FIGURE 1. Experiment setup used for formation of HIFU lesions using a single-element transducer attached to the of the tank with an imaging probe monitoring a cross section of the lesion through an acoustic window.

RESULTS AND DISCUSSION

The experimental setup shown in Figure 1 was used in obtaining images of *ex vivo* tissue samples before, during and after thermal lesion formation with the spherical therapy transducer. This setup was designed to allow comparisons with our a dual-mode 64-element ultrasound phased array operating at 1 MHz described in [3]. Results shown in [3] confirmed that echoes from the lesion location exhibited increased levels of second harmonic generation even at normal exposure conditions. In this paper, we show imaging results from a single-shot slightly overexposure condition of a 5 second pulse at 1800 W/cm^2. This exposure typically produces a cigar-shaped lesion with average length of 10 mm and slight widening of the lateral extent of the lesion at the base (nearer to the therapeutic transducer). This is part of a study for characterization of different imaging modes at a full range of exposure conditions.

Figure 2 shows the RF data along a line through the lesion before lesion formation (upper left). The figure also shows spectrograms of the RF data (showing the frequency content of the RF echoes, lower left). Echoes from the tissue sample begin at depth 135 mm. The results show that the echoes before lesion formation cover the bandwidth of the CA4121 probe (fundamental at 1.57 MHz and some 2nd harmonic). This is confirmed by the corresponding PI data shown on the right hand side, which shows the second harmonic data just above the noise level.

On the other hand, the spectrogram of the RF data shown in Figure 3 from the same direction after lesion formation show strong fundamental and 2nd harmonic components at the lesion location (145 mm). This is also very clear in the PI data which shows a strong 2nd harmonic at the same location. In addition, the PI data consistently showed a significant component at 2.2 MHz (believed to be an ultra harmonic component).

DETECTION AND MAPPING OF THERMAL LESIONS USING DUAL-MODE ULTRASOUND PHASED ARRAYS

Hui Yao, Pornchai Phukpattaranont, and Emad S. Ebbini

Department of Electrical and Computer Engineering
University of Minnesota
Minneapolis, MN 55455

ABSTRACT

It has long been recognized that thermal lesions formed using high-intensity focused ultrasound (HIFU) exhibit nonlinear behavior that can be detected in pulse-echo ultrasound. Second harmonic imaging of freshly formed thermal lesions have consistently shown significant enhancement in their visualization confirming this nonlinear behavior. In this paper, we describe a post-beamforming nonlinear filtering algorithm based on second-order Volterra filter (SVF) model that separates the linear and quadratic components of the echo signal leading to significant enhancement of lesion visualization. Images from *ex vivo* tissue samples are shown to demonstrate the level of contrast enhancement achieved with the SVF-based quadratic filter compared with standard echo and 2nd harmonic imaging results.

1. INTRODUCTION

Since early 2001, we have used a dual-mode array described in [1] to form HIFU-induced thermal lesions in freshly excised degassed tissue under a variety of *normal exposure* and *over exposure conditions*. Single-transmit focus images were collected for over 100 lesions before and after lesion formation. These images have consistently shown 5 - 7 dB enhancement in the echogenicity from the lesion location in the standard echographic images. These results were much more consistent than the reported "flashes" on the B-scan images when diagnostic ultrasound systems are used to monitor HIFU lesion formation. Motivated by the excellent investigation by P. P. Lele reported in [2], we hypothesized that this change in echogenicity is due to stable microbubbles that can occur even at low insonation levels. Lele found that subharmonic emission due to microbubbles showed a monotonic increase with intensity from 150 mW/cm^2 to 1500 W/cm^2 without a distinct threshold for emission (measurements done *in vitro* and *in vivo* at 2.7 and 1.8 MHz). The consistency of the increase in echogenicity at the lesion may be explained by the fact that the microbubbles may already be resonant at the imaging frequency (same as the therapeutic HIFU beam when the dual-mode array is is used), perhaps a result of rectified diffusion.

The standard echographic images at the fundamental, however, offer limited contrast enhancement due to the speckle phenomenon. Therefore, they could not provide a reliable method for mapping the boundaries of HIFU-induced lesions. This lead us to try to exploit the nonlinear nature of the microbubbles to enhance the visualization and mapping of thermal lesions. The idea was that, if microbubbles are indeed present at the lesion location, they will generate nonlinear echoes that may be better suited for mapping. We have initially investigated second harmonic (SH) imaging as a means of enhancing the lesion contrast for improving the visualization of these images. SH images of thermal lesions have shown increase in the contrast on the order of 22 - 25 dB, but with decreased dynamic range of the resulting images [1]. A post-beamforming nonlinear compounding algorithm was shown to improve the contrast in lesion echogenicity to 30 - 35 dB without loss in dynamic range [3]. This was achieved by compounding the fundamental and the SH images using spatial compounding functions based on the receive beamforming characteristics of the dual-mode array at the fundamental and the SH frequencies. In this paper, we describe a post-beamforming filtering algorithm for separating the linear and quadratic components of the beamformed data based on the SVF. This approach is superior to all of the algorithms based on SH imaging. It greatly enhances lesion to tissue contrast without any loss in spatial resolution. In addition, it enhances the dynamic range of the image thus greatly improving both detecting and mapping of HIFU-induced lesions, even for volumetric lesions.

2. IMAGE FORMATION

Figure 1 summarizes the image acquisition and image formation model. A 64-element array optimized for maximum energy delivery at 1 MHz (Imasonic, Besançon, France)

Funded by Grant DAMD 17-01-1-330 from the US Army Medical Research and Materiel Command and Esaote, S.p.A., Genoa, Italy.

0-7803-7582-3/02/$17.00

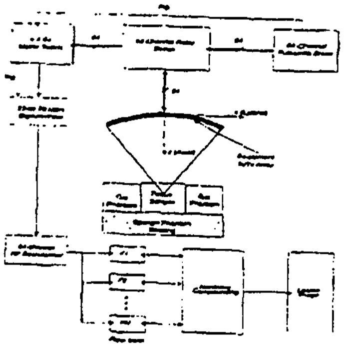

Fig. 1. Imaging Setup

is used for lesion formation in sample tissue. Lesions are formed by focusing the array at a point within the target and maintaining high-power output for time intervals on the order of seconds (1-5 seconds typical). The power is interrupted for short intervals (milliseconds) to acquire image data by transmitting short (μs) pulse from all 64-elements and receiving on selected elements using a matrix switch. Once the image data set is collected, RF beamforming is performed to form standard echographic images of the target region. Figure 1 also shows a general post-beamforming filter bank for analysis of beamformed data. For example, the filter bank could be designed to perform harmonic decomposition of beamfromed data (e.g., fundamental and 2nd harmonic imaging). Alternatively, the filter bank can be designed to separate the linear and quadratic (nonlinear) components based on the 2nd order Volterra model described below.

3. SECOND-ORDER VOLTERRA MODEL

Results from [4] have shown the validity of a second-order Volterra filer as a model for pulse-echo ultrasound imaging data from tissue mimicking media. In this section, the decomposition of received echo, i.e., output sequences only, into linear and quadratic components by using least-squares approach of second-order Volterra model will be considered and the detail of algorithm implementation to pulse-echo ultrasound imaging will be stated.

3.1. Signal Separation Model

The algorithm described in this section is adapted from [5]. The response of a quadratically nonlinear system, $y(n+1)$, can be predicted by a second-order Volterra model of past m values as follows:

$$\begin{aligned} y(n+1) &= y_L(n+1) + y_Q(n+1) \\ &\sum_{i=0}^{m-1} y(n-i)h_L(i) \\ &+ \sum_{j=0}^{m-1}\sum_{k=j}^{m-1} y(n-j)y(n-k)h_Q(j,k) + \varepsilon(n), \quad (1) \end{aligned}$$

where $h_L(i)$ is linear filter coefficients, $h_Q(j,k)$ represents quadratic filter coefficients and $\varepsilon(n)$ is a modelling error and/or a measurement noise which is assumed to be an independent, identically distributed(i.i.d) random variable with zero mean. That is, if the model coefficients are known, the echo signal can be decomposed into linear and quadratic components. The latter can be expected to better represent the quadratic response of the system than, say, the second harmonic component. The model coefficients can be obtained by setting the linear and quadratic prediction problem in Equation 1 to form a set of linear equations. Recognizing that the output is linear in terms of the (unknown) model coefficients, one obtains a matrix equation of the form:

$$\mathbf{f} = \mathbf{G}\mathbf{h} + \epsilon, \qquad (2)$$

where the vector $\mathbf{f}$, the matrix $\mathbf{G}$ and the error vector ϵ are

$$\begin{aligned} \mathbf{f} &= [y(n+1), y(n+2), \ldots, y(n+L)]^T \\ \mathbf{G} &= [\mathbf{y}(n), \mathbf{y}(n+1), \ldots, \mathbf{y}(n+L-1)]^T \\ \epsilon &= [\varepsilon(n), \varepsilon(n+1), \ldots, \varepsilon(n+L-1)]^T. \end{aligned}$$

where the data vector, $\mathbf{y}$, is given by:

$$\begin{aligned} \mathbf{y}(n) = [&y(n), y(n-1), y(n-2), \ldots, y(n-m+1), \\ &y^2(n), y(n)y(n-1), \ldots, y^2(n-m+1)]^T \end{aligned}$$

and the filter coefficient vector, $\mathbf{h}$, is given by:

$$\begin{aligned} \mathbf{h} = [&h_L(0), h_L(1), h_L(2), \ldots, h_L(m-1), \\ &h_Q(0,0), h_Q(0,1), \ldots, h_Q(m-1, m-1)]^T. \end{aligned}$$

The details of the solution for the coefficients of the SVF model can be found in [6]. Briefly, a minimum-norm least-squares solution of (2) is obtained using *truncated singular value decomposition, TSVD*. To assess the performance of the signal separation model in enhancing the lesion visualization, we compute the contrast-to-tissue ratio:

$$CTR = 10\log_{10}\left(\frac{\|\mathbf{y}_{QC}\|_2^2}{\|\mathbf{y}_{QT}\|_2^2}\right) \qquad (3)$$

where $\|\mathbf{y}_{QC}\|_2$ and $\|\mathbf{y}_{QT}\|_2$ are the l_2 norms of the quadratic components from the lesion and normal tissue regions, respectively. These regions are easily identified under various imaging conditions. For instance, for the application described in this paper, the contrast region is the expected location of the thermal lesion (often visible on the standard echographic image).

3.2. Implementation

The coefficients of the linear and quadratic components of the SVF model are obtained from the beamformed RF data. The implementation steps are as follows:

1. Using the standard echographic image, select a beamformed RF data segment from the expected lesion location.
2. Form the linear systems of equations according to (2).
3. Define contrast region (within the lesion) and normal tissue region for the computation of the mean-square error *MSE* and *CTR*.
4. Solve systems of linear equations by using TSVD regularization method.
5. Apply second-order Volterra filter to the beamformed RF data throughout the pulse-echo ultrasound image.
6. The quadratic component from the SVF can be displayed as a separate image or appropriately compounded with the linear component.

4. RESULTS AND DISCUSSION

The experimental setup shown in Figure 1 was used in obtaining images of *ex vivo* tissue samples before and after thermal lesion formation with a dual-mode 64-element ultrasound phased array operating at 1 MHz. The standard echographic images were formed by single transmit beams [1] along the main axis of the array and dynamic receive focusing at each pixel in the image. Results shown in [1] confirmed that echoes from the lesion location exhibited increased levels of second harmonic generation even at normal exposure conditions. Figure 2 shows the RF data along central axis of the dual-mode array before and after lesion formation at normal exposure level (850 W/cm^2 for 4 seconds). The figure also shows spectrograms of the RF data (showing the frequency content of the RF echoes in the axial direction). The results show that the echoes before lesion formation are centered at 1 MHz with no evidence of 2nd harmonic component in the tissue region (from 80 to 120 mm). On the other hand, the spectrogram of the RF data from the same direction after lesion formation shows a strong 2nd harmonic component at the lesion location (90 - 100 mm). Figure 3 shows the RF data along central axis of the dual-mode array before and after lesion formation at normal exposure level (2150 W/cm^2 for 3 seconds). The spectrograms show that the echoes before lesion formation are centered at 1 MHz with small 2nd harmonic component in the tissue region (at 100 mm). The spectrogram of the RF data from the same direction after lesion formation shows a strong 2nd harmonic component starting at 82 mm. This is consistent with the shape of the lesion determined by histological evaluation [1] (tear-drop cross section with the tip near the geometric center and the base near the front of the sample). It is interesting to note that, in addition to the increased 2nd harmonic generation, the echoes from the lesion appear to have wider bandwidth compared to echoes from the same location before lesion formation. This is reminiscent of the behavior of ultrasound contrast agents (UCAs). It provides indirect evidence that bubble oscillation occurs during and after lesion formation and lingers for tens of seconds (*in vitro* depending on lesion size).

In [1] we have shown images of single shot HIFU lesions at the fundamental and SH frequencies of the dual-mode transducer. Both imaging modes produced satisfactory images of the lesion in these cases, with the SH images providing higher contrast of lesion echogenicity. However, both of these methods suffer when imaging extended lesions. One such example is shown in Figure 4 before (left) and after lesion formation at the fundamental (top pair), SH (middle pair) and using the quadratic component from the SVF (bottom pair). One can easily observe the increase in echogenicity at the lesion location (90 - 100 mm along the axis of the array) for all three modes. However, one can see that the dynamic range of the fundamental image is limited by the speckle pattern from tissue surrounding the lesion while the SH image is limited by the beamforming artifacts. The lesion echogenicity in this case is nearly 17 dB above the normal tissue echogenicity in standard echographic image (typical contrast is more like 5 - 7 dB). The SH images improve the lesion contrast to approximately 25 dB compared to normal tissue (22 - 25 dB typical), but beamforming artifacts compromise the definition of the lesion boundaries in the lateral direction.

Using a beamformed echo data segment along the main axis of the array, the coefficients of linear and quadratic components of the SVF were estimated as described in Section 3.2. The quadratic components of the beamformed RF data were filtered out at all pixel locations. The images before and after lesion formation are shown in Figure 4 at 40 dB dynamic range. One can see quite clearly that the grating lobe components visible in the 2nd harmonic images are effectively eliminated in the quadratic component images obtained through the SVF. In addition, the speckle components conspicuous in the standard echo images is greatly reduced. This level of enhancement is typical and has been observed consistently in over 100 experiments similar to the one described in this paper. The reader can appreciate that the lesion boundaries are well defined in both the axial and lateral directions. With the significant increase in dynamic range, one can see that both detection and mapping of thermal lesions is significantly facilitated by the use of the quadratic filter based on the SVF model.

5. CONCLUSIONS

Experimental results from *ex vivo* tissue samples provide the strongest evidence yet that thermal lesions exhibit nonlinear behavior as a propagation medium. Using a the SVF

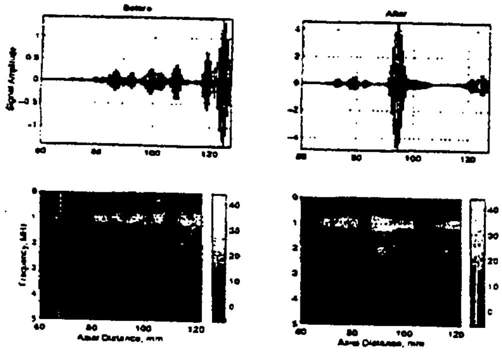

Fig. 2. RF data and spectrograms before(left) and after (right) *normal exposure.*

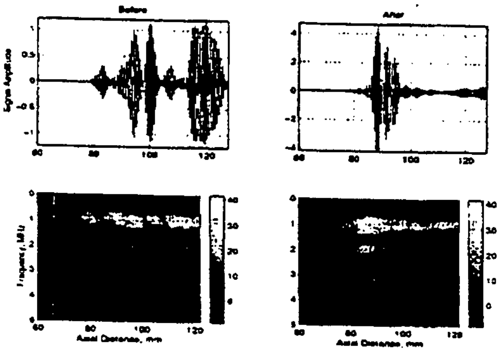

Fig. 3. RF data and spectrograms before (left) and after (right) *over exposure.*

model, we have separated the linear and quadratic components in the beamformed RF echo data and formed images from the quadratic components. The quadratic component images show significant enhancement in lesion visualization due to:

1. They directly exploit the nonlinear nature of freshly formed thermal lesion (possibly due to formation of microbubbles).
2. Quadratic component combines both low frequency (close to dc) and harmonic frequency in forming nonlinear echoes. This simultaneously reduces speckle and beamforming artifacts without loss in spatial resolution.
3. The quadratic kernel of the SVF rejects the additive white Gaussian noise components which significantly improves the SNR of the imaging system and enhances the visualization of low echogenicity regions in the image.

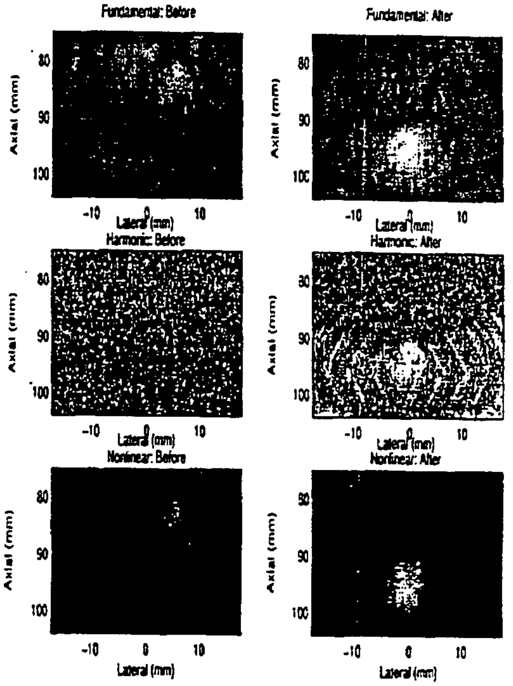

Fig. 4. Images before (left) and after (right) formation of lesion. Top: standard echo. Middle: second harmonic. Bottom: Quadratic.

6. REFERENCES

[1] E. Ebbini, J. Bischof, and J. Coad, "Lesion formation and visualization using dual-mode ultrasound phased array," in *2001 Ultrasonics Symposium*, 2001, vol. 2, pp. 1351–1354.

[2] M. H. Repacholi, M. Grandolfo, and A. Rindi, Eds., *Effects of ultrasound on solid mammalian tissue and tumors in* vivo, Plenum, London, 1987.

[3] C. Steidl, H. Yao, P. Phukpattaranont, and E. Ebbini, "Dual-mode ultrasound phased arrays for noninvasive surgery post-beamforming image compounding algorithms for enhanced visualization of thermal lesions," in *2002 Int. Symposium on Biomedical Imaging*, 2002, pp. 429–432.

[4] H. Yao, P. Phukpattaranont, and E. S. Ebbini, "Post-beamforming second-order volterra filter for nonlinear pulse-echo imaging," in *ICASSP*, 2002, vol. 2, pp. 1133–1136.

[5] K. Kim, S. B. Kim, E. J. Powers, R. W. Miksad, and F. J. Fischer, "Adaptive second-order volterra filtering and its application to second-order drift phenomena," *IEEE J. Oceanic Eng.*, vol. 19, no. 2, pp. 183–192, Apr. 1994.

[6] P. Phukpattaranont and E. Ebbini, "Post-beamforming volterra filter for contrast agent imaging," in *2002 Ultrasonics Symposium*, 2002, vol. 2.

Appendix 4

Nonlinear Imaging Methods for Characterization of HIFU-Induced Lesions

Hui Yao, Pornchai Phukpattaranont and Emad S. Ebbini

Department of Electrical and Computer Engineering
University of Minnesota, Minneapolis, MN 55455, USA

ABSTRACT

Nonlinear ultrasonic imaging methods (like pulse inversion[1] and quadratic imaging based second-order Volterra filter[8]) are used in visualization of lesion formation in freshly excised tissue. Both of these methods are more sensitive to nonlinear echoes (e.g., due to micro-bubbles) than standard B-mode imaging. While all three methods typically show increased echogenicity at the lesion location, the nonlinear methods exhibit more localized echo enhancement than B-mode imaging. Therefore, nonlinear methods are potentially better suited to lesion mapping for purposes of image guidance. Quadratic images have the added advantage of a significant increase in image dynamic range and noise reduction (a major limitation of pulse inversion imaging). The results shown in this report continue to support the hypothesis that micro-bubbles play an important role of lesion formation. In this paper, we present imaging results before and after volumetric lesion formation in *ex vivo* tissue. The results illustrate the advantage of nonlinear imaging methods compared to conventional B-scan imaging in terms of accurate mapping of lesion size and location.

Keywords: Noninvasive surgery, image guidance, treatment monitoring, ultrasonic imaging, phased arrays, autoregressive modelling.

1. INTRODUCTION

We have used a dual-mode array described in[2] to form HIFU-induced thermal lesions in freshly excised degassed tissue under a variety of *normal exposure* and *over exposure conditions*. Single-transmit focus images were collected for over 100 lesions before and after lesion formation. These images have consistently shown 5 - 7 dB enhancement in the echogenicity from the lesion location in the standard echographic images. These results were much more consistent than the reported "flashes" on the B-scan images when diagnostic ultrasound systems are used to monitor HIFU lesion formation. Motivated by the excellent investigation by P. P. Lele reported in,[5] we hypothesized that this change in echogenicity is due to stable microbubbles that can occur even at low insonation levels. Lele found that subharmonic emission due to microbubbles showed a monotonic increase with intensity from 150 mW/cm^2 to 1500 W/cm^2 without a distinct threshold for emission (measurements done *in vitro*

Other author information: E-mail: emad@ece.umn.edu

and *in vivo* at 2.7 and 1.8 MHz). The consistency of the increase in echogenicity at the lesion may be explained by the fact that the microbubbles may already be resonant at the imaging frequency (same as the therapeutic HIFU beam when the dual-mode array is is used), perhaps a result of rectified diffusion.

The standard echographic images at the fundamental, however, offer limited contrast enhancement due to the speckle phenomenon. Therefore, they could not provide a reliable method for mapping the boundaries of HIFU-induced lesions. This lead us to try to exploit the nonlinear nature of the microbubbles to enhance the visualization and mapping of thermal lesions. The idea was that, if microbubbles are indeed present at the lesion location, they will generate nonlinear echoes that may be better suited for mapping. We have initially investigated second harmonic (SH) imaging as a means of enhancing the lesion contrast for improving the visualization of these images. SH images of thermal lesions have shown increase in the contrast on the order of 22 - 25 dB, but with decreased dynamic range of the resulting images.[2] A post-beamforming nonlinear compounding algorithm was shown to improve the contrast in lesion echogenicity to 30 - 35 dB without loss in dynamic range.[7] This was achieved by compounding the fundamental and the SH images using spatial compounding functions based on the receive beamforming characteristics of the dual-mode array at the fundamental and the SH frequencies. In this paper, we use a commercial imaging scanner with modifications to allow pulse inversion imaging in addition to standard B-mode imaging for the visualization of freshly excised tissue before, during, and after the formation of HIFU lesions.

2. NONLINEAR IMAGING METHODS

2.1. Pulse Inversion Imaging

This method was recently introduced by Burns and coworkers[6] for enhancing contrast echoes in contrast-assisted pulse-echo imaging. The basic implementation of this method entails the use of two pulses per image line. These pulses are carefully designed such that, $p_2(t) = -p_1(t - T_L)$, where T_L is some appropriate delay (on the order of the pulse-echo time from the maximum depth of interest). Summing the echoes resulting from the two pulses eliminates the odd-harmonic components from the echo signal (including the fundamental) while doubling the even-harmonic (mostly second) components. This method currently represents the leading approach for contrast-agent imaging, especially with low concentration and/or very low transmit signals to minimize the generation of tissue nonlinearity.

2.2. Quadratic Imaging Based On SVF

We have recently developed a new nonlinear imaging system based on the SVF.[8] This has a number of advantages when compared to PI imaging (e.g. requires only a single pulse per line and increased dynamic range).

2.2.1. Second-Order Volterra Model

Results from[8] have shown the validity of a second-order Volterra filer as a model for pulse-echo ultrasound imaging data from tissue mimicking media. In this section, the decomposition of received echo, i.e., output sequences only, into linear and quadratic components by using least-squares approach of second-order Volterra model will be considered and the detail of algorithm implementation to pulse-echo ultrasound imaging will be stated.

2.2.2. Signal Separation Model

The algorithm described in this section is adapted from.[3] The response of a quadratically nonlinear system, $y(n+1)$, can be predicted by a second-order Volterra model of past m values as follows:

$$\begin{aligned} y(n+1) &= y_L(n+1) + y_Q(n+1) \\ &= \sum_{i=0}^{m-1} y(n-i)h_L(i) + \sum_{j=0}^{m-1}\sum_{k=j}^{m-1} y(n-j)y(n-k)h_Q(j,k) + \varepsilon(n). \quad (1) \end{aligned}$$

where $h_L(i)$ is linear filter coefficients, $h_Q(j,k)$ represents quadratic filter coefficients and $\varepsilon(n)$ is a modelling error and/or a measurement noise which is assumed to be an independent, identically distributed(i.i.d) random variable with zero mean. That is, if the model coefficients are known, the echo signal can be decomposed into linear and quadratic components. The latter can be expected to better represent the quadratic response of the system than, say, the second harmonic component. The model coefficients can be obtained by setting the linear and quadratic prediction problem in Equation 1 to form a set of linear equations. Recognizing that the output is linear in terms of the (unknown) model coefficients, one obtains a matrix equation of the form:

$$\mathbf{f} = \mathbf{G}\mathbf{h} + \epsilon, \qquad (2)$$

where the vector $\mathbf{f}$, the matrix $\mathbf{G}$ and the error vector ϵ are

$$\begin{aligned} \mathbf{f} &= [y(n+1), y(n+2), \dots, y(n+L)]^T \\ \mathbf{G} &= [\mathbf{y}(n), \mathbf{y}(n+1), \dots, \mathbf{y}(n+L-1)]^T \\ \epsilon &= [\varepsilon(n), \varepsilon(n+1), \dots, \varepsilon(n+L-1)]^T. \end{aligned}$$

where the data vector, $\mathbf{y}$, is given by:

$$\begin{aligned} \mathbf{y}(n) = [&y(n), y(n-1), y(n-2), \dots, y(n-m+1), \\ &y^2(n), y(n)y(n-1), \dots, y^2(n-m+1)]^T \end{aligned}$$

and the filter coefficient vector, $\mathbf{h}$, is given by:

$$\begin{aligned} \mathbf{h} = [&h_L(0), h_L(1), h_L(2), \dots, h_L(m-1), \\ &h_Q(0,0), h_Q(0,1), \dots, h_Q(m-1, m-1)]^T. \end{aligned}$$

The details of the solution for the coefficients of the SVF model can be found in.[4] Briefly, a minimum-norm least-squares solution of (2) is obtained using *truncated* *singular value decomposition. TSVD.* To assess the performance of the signal separation model in enhancing the lesion visualization, we compute the contrast-to-tissue ratio:

$$CTR = 10\log_{10}\left(\frac{\|\mathbf{y}_{QC}\|_2^2}{\|\mathbf{y}_{QT}\|_2^2}\right) \tag{3}$$

where $\|\mathbf{y}_{QC}\|_2$ and $\|\mathbf{y}_{QT}\|_2$ are the l_2 norms of the quadratic components from the lesion and normal tissue regions, respectively. These regions are easily identified under various imaging conditions. For instance, for the application described in this paper, the contrast region is the expected location of the thermal lesion (often visible on the standard echographic image).

2.2.3. Implementation

The coefficients of the linear and quadratic components of the SVF model are obtained from the beamformed RF data. The implementation steps are as follows:

1. Using the standard echographic image, select a beamformed RF data segment from the expected lesion location.
2. Form the linear systems of equations according to (2).
3. Define contrast region (within the lesion) and normal tissue region for the computation of the mean-square error *MSE* and *CTR*.
4. Solve systems of linear equations by using TSVD regularization method.
5. Apply second-order Volterra filter to the beamformed RF data throughout the pulse-echo ultrasound image.
6. The quadratic component from the SVF can be displayed as a separate image or appropriately compounded with the linear component.

3. EXPERIMENTAL SETUP

Figure 1 shows a simple arrangement for the formation of HIFU lesions in freshly excised and degassed porcine livers samples. The therapy transducer is a 1.5 MHz single-element spherical-shell transducer with a radius of curvature equal to its diameter and equal to 63.5 mm (Etalon, Lizton, Indiana). The transducer is fixed to the back of a small tank as shown and driven by a power amplifier (ENI, Rochester, NY) and a programmable function generator. This assembly can be used in generating a variety of amplitude-modulated HIFU bursts from tens of milliseconds to several seconds long and intensities up to 3000 W/cm^2 (conservative estimate).

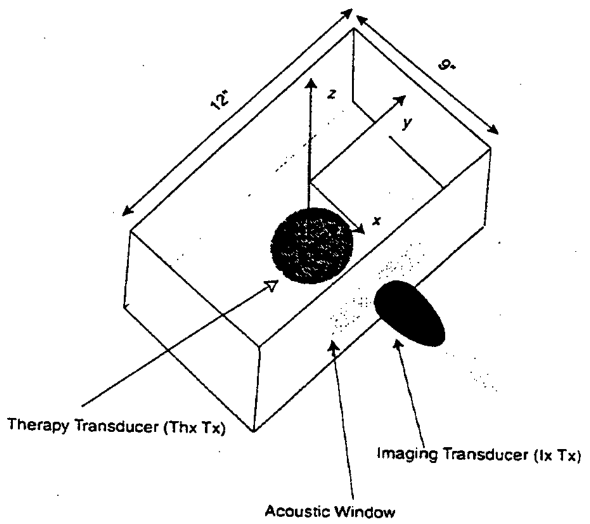

Figure 1. Experiment setup used for formation of HIFU lesions using a single-element transducer attached to the of the tank with an imaging probe monitoring a cross section of the lesion through an acoustic window.

3.1. Real-time Imaging

Real-time imaging is performed using a modified Technos MP system from ESAOTE. Genoa, Italy. The system is modified to allow imaging in pulse inversion mode in addition to normal B-mode imaging. In addition, a hardware module for capturing high-quality beamformed RF data allows us to capture and upload up to 60 seconds of full frame data with a specified frame rate. A CA 421 convex probe was used in acquiring image data for this paper. Image data was acquired in pulse inversion (PI) mode with a 2-cycle transmit pulse centered at 1.57 MHz. The imaging transducer was aligned so that the image plane is $x - y$ plane (to allow imaging a cross section of the lesion). However, imaging in the $x - z$ plane was often used, especially for imaging discrete (single-shot) lesions (to allow imaging the lesion along the axis of the therapeutic array).

3.2. Lesion Formation

Volumetric lesions were formed by continuously driving the therapy transducer while moving the sample holder in a raster scan with the stepper motor. The motor speed, input voltage profile, and line spacing in the raster were changed to produce a variety of volumetric lesions that can be characterized as *over exposure*, *normal exposure* or *under exposure*.

4. RESULTS AND DISCUSSION

The experimental setup shown in Figure 1 was used in obtaining images of *ex vivo* tissue samples before and after thermal lesion formation with the spherical therapy transducer. This setup was designed to allow comparisons with our a dual-mode 64-element ultrasound phased array operating at 1 MHz described in.[2] Results shown in[2] confirmed that echoes from the lesion location exhibited increased levels of second harmonic generation even at normal exposure conditions. In this paper, we show imaging results from continuous exposure at 1800 W/cm^2 while the tissue is moved in a raster scan 10 × 10 mm with raster lines parallel to the face of the imaging transducer (1 mm spacing). The motor speed was set at 2 mm/s thus giving an exposure time of roughly 1 second at one location in the focal plane of the therapeutic transducer, but larger in the prefocal region. Figure 2 shows a cross section of the tissue after lesion formation with conspicuous thermal lesion in the upper left corner. The cross section conforms approximately to the programmed pattern with distortions most probably due to deformation of tissue as it was cut without fixing. The tissue is positioned so that the therapeutic transducer is aimed upwards into the imaging plane and the imaging transducer is imaging downwards. Gross measurements of the cross section of the lesion shows a lateral extent of 10 mm and an axial extent of 12 (with respect to the imaging transducer).

Figure 3 shows B-mode (left), PI (center), and quadratic (right) images before (top) and after lesion formation. All imaging modes show enhanced echogenicity at the lesion location at an axial distance of 145 mm from the imaging transducer. The PI and quadratic images show a smaller size hyperechoic region with lateral extent of about 12 mm compared to 13 mm in the B-mode image. The axial extent of the hyperechoic region is 11 mm in the PI image and 10 mm in the quadratic image. It was difficult to determine this value in the B-mode image due to the interference of the speckle pattern in tissue. This result is typical, i.e. the PI data gives a more accurate map of the lesion than B-mode data.

Comparing the quadratic and B-mode images, one can see the speckle components conspicuous in the standard echo images is greatly reduced. This level of enhancement is typical and has been observed consistently in over 100 experiments similar to the one described in.[2] The reader can appreciate that the lesion boundaries are well defined in both the axial and lateral directions. With the significant increase in dynamic range, one can see that both detection and mapping of thermal lesions is significantly facilitated by the use of the quadratic filter based on the SVF model. It is also interesting to not the remarkable similarity between the PI and quadratic images, except that the latter has more than twice the dynamic range. These results are also typical and represent the potential advantage of the quadratic processing versus pulse inversion. The result can be understood by keeping in mind that both methods are sensitive to the harmonic content of the RF data, but they differ in their respective degrees of suppressing the noise component; the quadratic signal being far superior in this respect.

Figure 2. A section of a volumetric lesion in an *ex vivo* porcine liver sample.

5. CONCLUSIONS

Experimental results from *ex vivo* tissue samples provide compelling evidence that thermal lesions exhibit nonlinear behavior as a propagation medium. Nonlinear imaging methods were used to separate the linear and nonlinear components in the beamformed RF echo data. PI images confirmed the presence of strong 2nd harmonic component in echoes from lesion location. The quadratic component images (obtained through SVF) show significant enhancement in lesion visualization due to:

1. They directly exploit the nonlinear nature of freshly formed thermal lesion (possibly due to formation of microbubbles).
2. Quadratic component combines both low frequency (close to dc) and harmonic frequency in forming nonlinear echoes. This simultaneously reduces speckle and beamforming artifacts without loss in spatial resolution.
3. The quadratic kernel of the SVF rejects the additive white Gaussian noise components which significantly improves the SNR of the imaging system and enhances the visualization of low echogenicity regions in the image.

Efforts to further characterize echo signals from the different imaging methods and correlate them to the state of the tissue are currently underway.

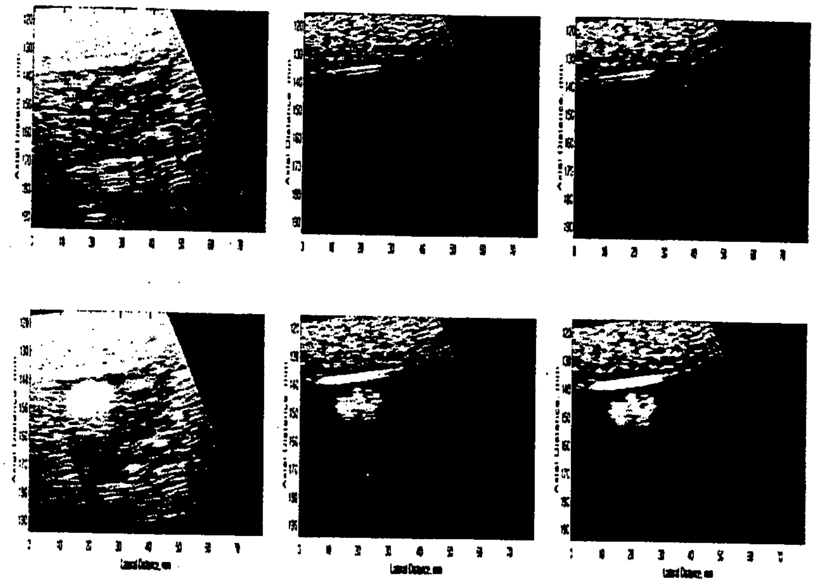

Figure 3. B-mode (left), pulse inversion (center), and Quadratic images before (upper) and immediately after (lower) formation of volumetric lesion. Dynamic range: B-mode 60dB, PI 30 dB, Quadratic 75 dB.

Acknowledgments

Funded by Grant DAMD 17-01-1-330 from the US Army Medical Research and Materiel Command and Esaote, S.p.A., Genoa, Italy.

REFERENCES

1. P. N. Burns, S. R. Wilson, and D. H. Simpson. Pulse inversion imaging of liver blood flow: Improved method for characterizing focal masses with microbubble contrast. *Invest Radiol*, 35(1):58-71, 2000.
2. E. Ebbini, J. Bischof, and J. Coad. Lesion formation and visualization using dual-mode ultrasound phased array. In *2001 Ultrasonics Symposium*, volume 2, pages 1351 1354, 2001.
3. K. Kim, S. B. Kim, E. J. Powers, R. W. Miksad, and F. J. Fischer. Adaptive second-order volterra filtering and its application to second-order drift phenomena. *IEEE J. Oceanic Eng.*, 19(2):183 192, Apr. 1994.
4. P. Phukpattaranont and E. Ebbini. Post-beamforming volterra filter for contrast agent imaging. In *2002 Ultrasonics Symposium*, volume 2, 2002.
5. M. H. Repacholi, M. Grandolfo, and A. Rindi, editors. *Effects of ultrasound on solid mammalian tissue and tumors* in vivo. Plenum, London, 1987.

6. D. H. Simpson, C. T. Chin, and P. N. Burns. Pulse inversion doppler: A new method for detecting nonlinear echoes from microbubble contrast agent. *IEEE Trans. Ultrason., Ferroelect., Freq. Contr.*, 46(2):372–382, Mar. 1999.
7. C. Steidl, H. Yao, P. Phukpattaranont, and E. Ebbini. Dual-mode ultrasound phased arrays for noninvasive surgery post-beamforming image compounding algorithms for enhanced visualization of thermal lesions. In *2002 Int. Symposium on Biomedical Imaging*, pages 429–432, 2002.
8. H. Yao, P. Phukpattaranont, and E. S. Ebbini. Post-beamforming second-order volterra filter for nonlinear pulse-echo imaging. In *ICASSP*, volume 2, pages 1133–1136, 2002.

Appendix 5

IEEE TRANSACTIONS ON ULTRASONICS, FERROELECTRICS, AND FREQUENCY CONTROL, DRAFT

Postbeamforming Second-Order Volterra Filter for Pulse-Echo Ultrasonic Imaging

Pornchai Phukpattaranont and Emad S. Ebbini, *Member, IEEE*

***Abstract*—We present a new algorithm for deriving a second-order Volterra filter (SVF) capable of separating linear and quadratic components from echo signals. Images based on the quadratic components are shown to provide contrast enhancement between tissue and ultrasound contrast agents (UCAs) without loss in spatial resolution. It is also shown that the quadratic images preserve the low scattering regions due to their high dynamic range when compared with standard B-mode or harmonic images. A robust algorithm for deriving the filter has been developed and tested on real-time imaging data from contrast and tissue-mimicking media. Illustrative examples from image targets containing contrast agent and tissue-mimicking media are presented and discussed. Quantitative assessment of the contrast enhancement is performed on both the RF data and the envelope-detected log-compressed image data. It is shown that the quadratic images offer levels of enhancement comparable or exceeding those from harmonic filters while maintaining the visibility of low scattering regions of the image.**

I. INTRODUCTION

INCREASING interest in extending the capabilities of ultrasound imaging by utilizing ultrasound contrast agents (UCAs) has heightened the need for more suitable imaging techniques. In standard B-mode imaging, UCAs increase the echogenicity from perfused tissues [1]. This results in improved endocardial border detection in left ventricular opacification, which leads to a better analysis of wall motion abnormalities [2]. Nevertheless, in the myocardium where the ratio of blood volume to tissue is quite low (approximately 10% [3]), the backscatter from the small number of microbubbles in vessels can be dominated by echoes from surrounding tissue. In this occurrence, standard B-mode imaging offers inferior UCA detectability in the presence of tissue, stated as agent-to-tissue ratio [4]. In order to increase the sensitivity of UCA detections, various new imaging techniques [5], [6] have been developed by employing some specific acoustic signatures of UCAs, such as nonlinear and transient scattering.

Imaging techniques based on nonlinear oscillations have been designed for separating and enhancing nonlinear UCA echoes from a specified region of interest within the imaging field, including second harmonic (SH) B-mode imaging and pulse inversion (PI) Doppler imaging [7]. The SH imaging employs a fundamental frequency transmit pulse and produces images from the second harmonic component of received echoes by using a second harmonic bandpass filter (BPF) to remove the fundamental frequency. In order to increase UCA detection sensitivity in the limited transducer bandwidth condition, spectral overlap between fundamental and second harmonic parts need to be minimized by transmitting narrow-band pulses resulting in an inherent tradeoff between contrast and spatial resolution.

In PI imaging, a sequence of two inverted acoustic pulses with appropriate delay is transmitted into tissue. Images are produced by summing the corresponding two backscattered signals. In the absence of tissue motion, the resulting sum can be shown to contain only even harmonics of the nonlinear echoes [7]. The PI imaging overcomes the tradeoff between contrast and spatial resolution because it utilizes the entire bandwidth of the backscattered signals [7]. As a result, superior spatial resolution can be achieved when compared with SH imaging. Moreover, it has been shown that PI imaging can be operated in a continuous imaging mode with low mechanical indices (MIs) [8]. The PI imaging is sensitive to tissue motion because it is a multiple pulse technique; therefore, PI detection is combined with Doppler detection leading to a new technique called PI Doppler. The PI Doppler utilizes the advantages from both detection schemes and circumvents the tissue motion problem [7]. Nevertheless, an inherent multipulse technique of PI imaging results in the reduction of imaging frame rates.

In order to detect backscattered signals due to UCAs in pulse-echo ultrasound imaging with single transmit pulse per line and overcome the tradeoff between contrast and spatial resolution, we have developed a new imaging technique based on the Volterra filter [9]. The Volterra filter is a dynamic filter that operates in parallel on the linear, quadratic, cubic, etc., signal components to produce its output. It has a discrete convolutional form with finite memory that is commonly used in nonlinear DSP **[AU: Define DSP on first use.]** applications [10]. While the Volterra filter output is nonlinear in terms of the input data, it is linear in terms of its coefficients. As a result, linear processing can be applied to identify Volterra kernels (i.e., filter coefficients). The identification of Volterra kernels has been demonstrated in several applications [10], [11]. For example, the linear and quadratic Volterra kernels identified by an adaptive filtering algorithm based on recursive least-squares approach of a second-order Volterra

Manuscript received October 23, 2002; accepted March 21, 2003. This work is funded in part by a grant from Esaote, S.p.A., Genoa, Italy and by Grant DAMD 17-01-1-330 from the U.S. Army Medical Research and Materiel Command.

The authors are with the Electrical and Computer Engineering Department, University of Minnesota, MN (e-mail: emad@ece.umn.edu).

model are applied to separate the linear and quadratic responses of a tension leg platform [12].

In this paper, we present postbeamforming nonlinear filter based on the second-order Volterra filter (SVF). The filter is capable of separating linear and quadratic components from UCA-backscattered signals. Filter coefficients can be identified by forming a system of linear equations from a beamformed RF data segment in the UCA or tissue region and obtained by solving a minimum-norm least-squares (MNLS) problem. It is shown that the system identification approach to a nonlinear ultrasonic imaging is robust and can be applied to form nonlinear images throughout the imaging field, i.e., not confined to the region where the filter coefficients were derived. Images produced from quadratic output of the SVF model exhibit excellent contrast enhancement without loss in spatial resolution. In addition, quadratic images have increased dynamic range compared to standard B-mode and harmonic images allowing the preservation of image features along with contrast improvement.

II. Theory

For simplicity and without loss of generality, we illustrate the nonlinear postbeamforming algorithm using the SVF model. The algorithm described in this section for deriving the filter coefficients of the SVF extends to higher order in a straightforward manner. Initial experience with this model indicate that it is largely sufficient for tissue response. Furthermore, the SVF is computationally feasible for real-time application with today's technology, which makes it more attractive from the implementation point of view.

A. Second-Order Volterra Model

Results from [9] have shown the validity of a SVF as a model for pulse-echo ultrasound pulse-echo data from tissue mimicking media. An input-output system identification approach was used to estimate the coefficients of the linear and quadratic components of the SVF in the frequency domain. However, while the system identification study was necessary to establish the applicability of SVF to ultrasound pulse-echo data, it is not useful for imaging purposes as it requires access to both the input and the echo data from distinct scatterers in the tissue-mimicking media. An appropriate approach for imaging operates on the beamformed RF data to separate the linear and quadratic components regardless of the input. This signal separation approach allows us to extract the linear and quadratic signal components from the beamformed data to form linear and/or quadratic images separately or compounded. In this paper, we emphasize the quadratic images obtained from the SVF model based on a linear and quadratic prediction model of beamformer output described in the remainder of this section.

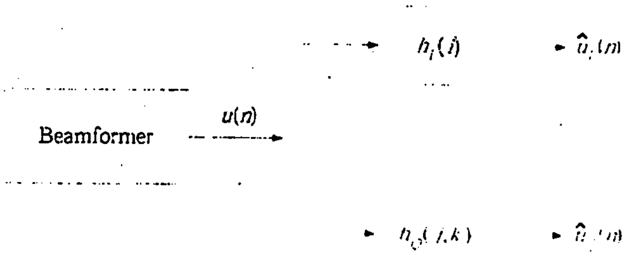

Fig. 1. Separation of beamformed RF data into linear and quadratic components using the SVF.

1. Signal Separation Model: Fig. 1 shows a simple block diagram of the imaging system based on SVF. The SVF operates on the beamformer output to produce the linear and quadratic components, $\hat{u}_L(n)$ and $\hat{u}_Q(n)$, respectively. Estimates of the total beamformer output can be obtained from these components simply by adding them

$$\hat{u}(n) = \hat{u}_L(n) + \hat{u}_Q(n), \tag{1}$$

where $\hat{u}(n)$, $\hat{u}_L(n)$, and $\hat{u}_Q(n)$ are the total, linear, and quadratic estimations, respectively. The separation of the linear and quadratic components can be achieved once the coefficients of the kernels, $h_L(i)$ (linear), and $h_Q(j,k)$ (quadratic) are found. In the following subsection, we describe a MNLS approach for determining these coefficients.

2. The MNLS Estimation of SVF Coefficients: The response of a quadratically nonlinear system with memory, $\hat{u}(n+1)$ can be predicted by a (discrete) second-order Volterra model operating on the m past samples as follows

$$\hat{u}(n+1) = \sum_{i=0}^{m-1} u(n-i)h_L(i) + \sum_{j=0}^{m-1}\sum_{k=j}^{m-1} u(n-j)u(n-k)h_Q(j,k), \tag{2}$$

where $h_L(i)$ is linear filter coefficients, and $h_Q(j,k)$ represents quadratic filter coefficients. Note that while $\hat{u}(n+1)$ is nonlinear with respect to the beamformed data, it is linear with respect to the coefficients of the linear and quadratic kernels of the SVF. Recognizing this fact, one can rewrite (2) in vector form

$$\hat{u}(n+1) = \mathbf{u}^T(n)\mathbf{h}, \tag{3}$$

where the data vector, $\mathbf{u}(n)$, is defined at sample n as

$$\mathbf{u}(n) = [u(n), u(n-1), u(n-2), \ldots, u(n-m+1), u^2(n), u(n)u(n-1), \ldots, u^2(n-m-1)]^T,$$

and the filter coefficient vector, $\mathbf{h}$, can be expressed as

$$\mathbf{h} = [h_L(0), h_L(1), h_L(2), \ldots, h_L(m-1), h_Q(0,0), h_Q(0,1), \ldots, h_Q(m-1, m-1)]^T;$$

where m is the system order and superscript ^{T} denotes the transpose. The total number of independent filter coefficients, N, is equal to $(m^2 + 3m)/2$ assuming a symmetrical quadratic kernel (i.e., $h_Q(j,k) = h_Q(k,j)$). Similarly, $\hat{u}(n+2), \hat{u}(n+3), \ldots, \hat{u}(n+M)$ can be represented in the form of (3) and expressed in the matrix form

$$\mathbf{f} = \mathbf{GH}, \qquad (4)$$

where the vector $\mathbf{f}$ and the matrix $\mathbf{G}$ are defined as

$$\mathbf{f} = [u(n+1), u(n+2), \ldots, u(n+M)]^T$$

and

$$\mathbf{G} = [\mathbf{u}(n), \mathbf{u}(n+1), \ldots, \mathbf{u}(n+M-1)]^T,$$

where M is the number of linear equations (observations). The linear and quadratic filter coefficients can be estimated by seeking an appropriate solution of (4). Well-known solutions to (4) are the least squares (LS) solution for the overdetermined case (more constraints than unknowns) and the minimum norm (MN) solution in the underdetermined case (less constraints than unknowns). A MNLS solution can be obtained by

$$\mathbf{h}_{\mathrm{MNLS}} = \mathbf{G}^{\dagger}\mathbf{f}. \qquad (5)$$

where $\mathbf{G}^{\dagger}$ is a generalized inverse [13]. This solution applies to both the overdetermined and underdetermined cases as it accounts for the effective rank of the matrix $\mathbf{G}$. In general, $\mathbf{G}$ could be rank deficient, i.e., has rank $r \leq \min\{M, N\}$. When this is the case, there are infinite number of solutions to (4) that produce the same LS error, $\|\mathbf{f} - \mathbf{G}\mathbf{h}_{LS}\|^2$. The MNLS is the unique solution to (4) with minimum norm, i.e., $\|\mathbf{h}_{\mathrm{MNLS}}\|^2 < \|\mathbf{h}_{LS}\|^2 \; \forall \, \mathbf{h}_{LS}$. The singular value decomposition (SVD) of $\mathbf{G}$ is given by

$$\begin{aligned} \mathbf{G} &= \mathbf{U}\mathbf{\Sigma}\mathbf{V}^T \\ &= \sum_{i=1}^{r} \sigma_i \mathbf{u}_i \mathbf{v}_i^T, \end{aligned} \qquad (6)$$

and

$$\begin{aligned} \mathbf{G}^{\dagger} &= \mathbf{V}\mathbf{\Sigma}^{\dagger}\mathbf{U}^T \\ &= \sum_{i=1}^{r} \frac{1}{\sigma_i} \mathbf{v}_i \mathbf{u}_i^T. \end{aligned} \qquad (7)$$

where $\mathbf{\Sigma}$ is a $M \times N$ diagonal matrix with singular values $\sigma_1 \geq \sigma_2 \geq \ldots \geq \sigma_r > \sigma_{r+1} = \ldots = \sigma_p = 0$ ($p = \min\{M, N\}$). The matrices $\mathbf{U}$ ($M \times M$) and $\mathbf{V}$($N \times N$) are formed from the columns $\{\mathbf{u}_i\}_{i=1}^{M}$ and $\{\mathbf{v}_i\}_{i=1}^{N}$, which are the orthogonal eigenvectors of $\mathbf{G}\mathbf{G}^T$ and $\mathbf{G}^T\mathbf{G}$, respectively [13]. Using (7), the MNLS solution to (5) is then given by

$$\mathbf{h}_{\mathrm{MNLS}} = \sum_{i=1}^{r} \frac{\mathbf{u}_i^T \mathbf{f}}{\sigma_i} \mathbf{v}_i. \qquad (8)$$

Note that, if $\mathbf{G}$ is full rank, the MNLS is equivalent to the LS solution in the overdetermined case and to the MN solution in the underdetermined case. For example, for $M < N$ (underdetermined), $\mathbf{h}_{\mathrm{MNLS}} = \mathbf{h}_{MN} = \mathbf{G}^T(\mathbf{G}\mathbf{G}^T)^{-1}\mathbf{f}$.

B. Regularization

The SVD of $\mathbf{G}$ forms a basis for regularization by appropriate selection of singular modes that enhance the reconstructed image in some sense. There are a number of approaches for regularization of (8), including single parameter and rank reduction regularization [14]. The latter, sometimes referred to as the truncated singular value decomposition (TSVD), produces a solution by truncating the number of singular modes of $\mathbf{G}$ with the smallest singular values below a certain threshold. The kth order TSVD solution is given by

$$\mathbf{h}_k = \sum_{i=1}^{k} \frac{\mathbf{u}_i^T \mathbf{f}}{\sigma_i} \mathbf{v}_i. \qquad (9)$$

where the truncation parameter $k \leq r$, also known as the rank of the approximation, is the number of singular modes used to compute the estimate.

The regularization is guided by the mean square error criterion, approximated by

$$\hat{E}(k) = 10 \log_{10} \left(\frac{\| \mathbf{f} - \mathbf{G}\mathbf{h}_k \|^2}{M} \right). \qquad (10)$$

where $\| \cdot \|^2$ is the l_2 norm.

In the context of the linear and quadratic prediction approach taken in this paper, the MSE decreases monotonically with k. A criterion for choosing an appropriate value of k is needed. In the context of contrast-agent imaging, an obvious criterion is the contrast-to-tissue ratio (CTR)

$$\mathrm{CTR} = 10 \log_{10} \left(\frac{\overline{P}_C}{\overline{P}_T} \right). \qquad (11)$$

where $\overline{P}_C$ is the average power of signals in a UCA region, and $\overline{P}_T$ is the average power of signals in a tissue region. The average power of signals in a given region, $\overline{P}$, can be expressed as

$$\overline{P} = \frac{1}{IJ} \left(\sum_{i=1}^{I} \sum_{j=1}^{J} x_{ij}^2 \right). \qquad (12)$$

where x_{ij} is the signal in that region. Note that the CTR used in this algorithm is determined from quadratic components of the SVF model. The CTR provides a meaningful stopping criterion for TSVD since $E(k)$ is monotonically decreasing or nonincreasing with k.

One may use a variety of methods to obtain a regularized solution to the set of equations involving the Volterra kernels. Examples are linear or nonlinear programming in cases when certain constraints on the filter coefficients are known to apply (e.g., positivity) or penalized maximum likelihood when known statistical properties of the data can be incorporated. A powerful approach seeks a solution to a constrained optimization problem of the form

$$\min_{\mathbf{h}_Q} \quad R^2 \qquad \text{subject to} \qquad \mathbf{G}\mathbf{h} = \mathbf{f}. \qquad (13)$$

where R^2 is an appropriately chosen quadratic ratio to be minimized (e.g., inverse of CTR) For example, R^2 can be chosen to reflect the inverse of the CTR before log compression. In general, it can be any quantity that depends on the solution $\mathbf{h_Q}$ that is to be minimized. This leads to a modified form of the TSVD given here

$$\mathbf{h}_k = \sum_{i=1}^{k} \frac{\sigma_i}{\sigma_i^2 + \gamma R_i^2} \mathbf{u}_i^T \mathbf{f} \mathbf{v}_i, \tag{14}$$

where γ is an appropriately chosen threshold, and R_i^2 is quadratic ratio resulting from the quadratic kernel obtained from the ith singular mode. Regardless of the regularization procedure, the fundamental result here is the use of the linear/quadratic prediction to obtain a set of independent equations that can be solved robustly to obtain the Volterra filter kernels.

C. Quadratic Images

Quadratic images are obtained from quadratic components of the second-order Volterra model. The coefficients of the SVF are derived from the beamformed RF data taken from a representative region on a standard B-mode image Details of the algorithm to produce the quadratic image are as follows.

From the standard B-mode image, a UCA region and a tissue region are defined for the CTR computation. The definition of the CTR reference regions depends on the imaging target are described in Section III-C. In general, we try to find regions at the same depth and with the same beam angle with respect to the axis of the imaging array. Furthermore, whenever possible, we chose multiple overlapping subregions to obtain multiple CTR values at different depths.

Once the CTR reference regions are defined, a segment of RF data from an axial line is selected to form a system of linear equations according to (4). This segment can be selected from the tissue or the UCA region as long as the appropriate regularization of the MNLS solution is sought. For example, when TSVD is used for regularization, CTRs of quadratic signals calculated from various orders of TSVD solutions are collected. With a defined range of system orders, a CTR plane as a function of truncation parameters and system orders is determined. Filter coefficients for the quadratic imaging generation are obtained from a truncation parameter and a system order that give the highest CTR value in the CTR plane. Of course, the TSVD approach can be used to obtain the coefficients of the quadratic kernel, $h_Q(i, j)$, for a predetermined filter order m. This may be necessary from the implementation point of view, when the size of the kernel is to be kept at manageable level. The results presented in this paper are obtained with low-order filter to emphasize the practicality of the Volterra filter approach.

The quadratic image is produced by applying the quadratic filter coefficients to the beamformed RF data throughout the standard B-mode image to estimate the quadratic component

$$\hat{u}_Q(n+1) = \sum_{j=0}^{m-1} \sum_{k=j}^{m-1} u(n-j)u(n-k)\hat{h}_Q(j, k), \tag{15}$$

where $\hat{h}_Q(j, k)$ is the estimated quadratic kernel (extracted from $\mathbf{h}_{\mathrm{MNLS}}$). A flowchart of this algorithm is shown in Fig. 2.

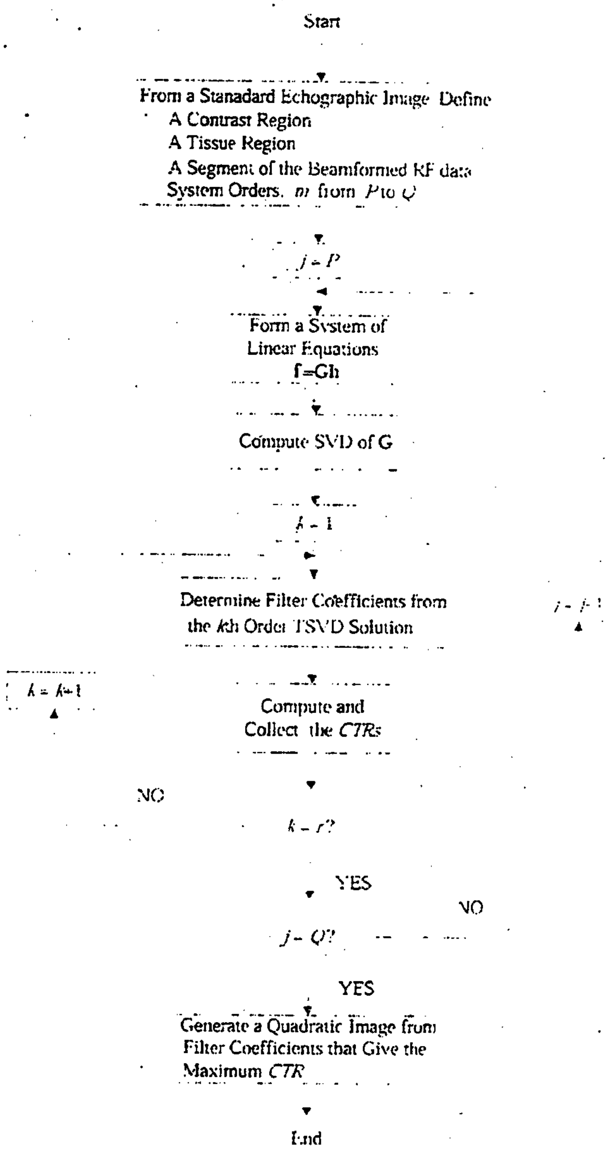

Fig 2 A flowchart of the algorithm for quadratic image generation.

D. Harmonic Imaging

Second harmonic imaging is based on filtering the RF data with a zero-phase linear BPF centered at twice the fundamental with restricted bandwidth to minimize the overlap between the fundamental and the second harmonic. The approach is appropriate for native harmonic imaging. However, when imaging UCA, the echo data from the UCA regions tends to have wider bandwidth when compared with echoes from tissue regions. Therefore, to obtain the highest possible contrast with a linear harmonic filter, we varied both the center frequency and the bandwidth of the filter and computed a CTR plane as a function of these parameters. This approach produced superior results compared to standard SH imaging. Harmonic imaging results shown in Section IV are obtained with the optimal linear BPF designed using the Parks-McClellan algorithm [18]. All linear filters used in this paper were implemented in a zero-phase realization ($y(n) = h(n) * h(-n) * x(n)$ or $Y(f) = |H(f)|^2 X(f)$) The order of the filter was chosen to achieve 50 dB stopband attenuation and 0.5 passband ripple.

III. Materials and Methods

Imaging results shown below demonstrate the contrast enhancement achieved by the postbeamforming SVF in the context of contrast-agent imaging in tissue-mimicking media. Two imaging targets with two imaging probes are used to demonstrate generality and robustness of the approach.

A. *Contrast Agent*

The contrast agent, BR14 (Bracco Research S.A., Geneva, Switzerland), was used. The BR14 is a new experimental agent that consists of high molecular weight gas bubbles encapsulated by a flexible phospholipid shell A 0.125 mL sample of BR14, prepared with 5 mL of 0.9% saline, was diluted in 500 mL of 0.9% saline leading to a 1:4000 dilution. In addition to BR14, cellulose particles (Sigma Cell Type 20, Sigma Chemical Co., St. Louis, MO) were used as linear scatterers in the flow channel target described below.

B. *Imaging Targets*

Images of two targets from two experimental setups were used to evaluate the performance of the quadratic imaging technique. The first experimental setup is shown in Fig. 3. The target is the L-shaped tissue-mimicking phantom in a beaker containing a dilution of BR14. The BR14 was constantly stirred by a magnetic stirrer. A MEGAS scanner (ESAOTE S.p.A., Genova, Italy) equipped with a 2-MHz phased array probe was used for image acquisition. The RF data acquisition was performed with 15-bit resolution at 40-MHz sampling frequency and without time gain control (TGC). This experiment allowed us to compare echoes from three different locations: the L-shaped tissue-mimicking phantom, the BR14, and the echo-free region visible in the scan. The significance of the latter is that any signal components observed in this region are largely artifacts from beamforming and/or reverberation. It should be noted, however, that there may be a small backscatter component present due to the beam reflections at the beaker, but this is hard to quantify in the presence of the contrast agent. Despite this limitation, it is interesting to compare the nature of the image pixels in this region from the three imaging methods.

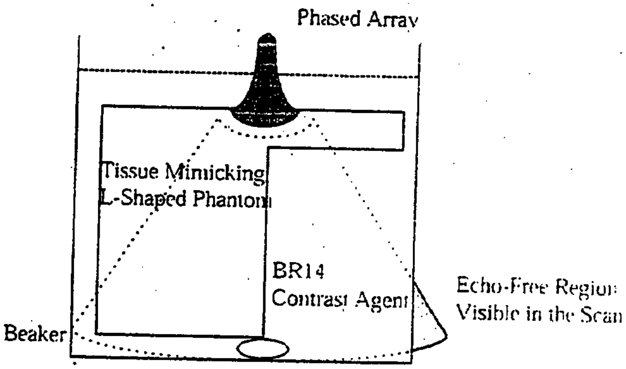

Fig. 3. Schematic for the imaging setup for the L-shaped phantom surrounded by the UCA.

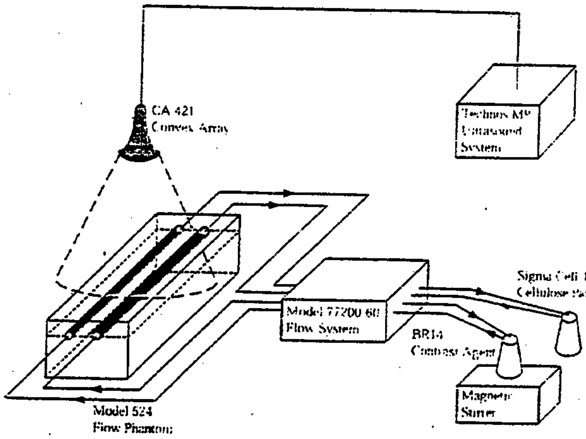

Fig. 4. The imaging setup for the flow phantom.

The second experimental setup, shown in Fig. 4 was used in obtaining images of a flow phantom (Model 524: ATS Laboratories, Inc., Bridgeport, CT) containing four flow channels with diameters 2, 4, 6, and 8 mm embedded in rubber-based tissue mimicking material. The flow phantom was connected to a flow system with a roller pump (Model 77200-60: Cole-Parmer Instrument Co., Vernon Hills, IL). Subsequently, the diluted BR14 and cellulose particles were circulated. In addition, the diluted BR14 was constantly stirred in a beaker using a magnetic hot plate stirrer (EW-84303-20: Corning Inc Corning, NY).

This experiment was designed to compare linear backscattered signals from cellulose in the 8-mm diameter flow channel with nonlinear backscattered signals from BR14 in the 6-mm diameter flow channel. The RF data were recorded and saved for later processing by the Technos MP ultrasound system (ESAOTE S.p.A., Genova, Italy) with a convex array probe (CA421: ESAOTE S.p.A., Genova, Italy) located perpendicularly to both the UCA and the cellulose flow channels. The RF data were acquired with 16-bit resolution at 20-MHz sampling frequency and without TGC. A 3-cycle pulse at 3.13 MHz was transmitted to produce standard B-mode images.

C. *Quantitative Analysis*

After the RF data corresponding to standard B-mode images were collected from experimental setups described above, quadratic images were obtained using the algorithm described in Section II-C. For comparison, harmonic images were produced by filtering the standard B-mode image with bandpass filters with center frequencies and fractional bandwidths chosen to maximize the CTR (defined by (11)) as described in Section II-D.

1. CTR Computations: The CTR was used for comparison between the image data in the RF domain before scan conversion as described in (11). Size and location of reference regions for each target are as follows. For the L-shape phantom, 45-mm axial segments of 20 adjacent A-lines on the tissue side and the same number on the contrast side were used. This phantom provided an excellent opportunity to compute CTR at multiple regions in the contrast and tissue regions with the same depth and the same beam angle from the axis of the imaging array. The calculation region extends by 45 mm in the axial direction (from 50 mm to 95 mm) and comprises 20 adjacent A-lines of RF data before scan conversion. The CTR values are calculated from cells with 3.8-mm axial extent with 10 connected A-lines and 50% overlap in both directions. For the flow phantom, one contrast region is in UCA flow channel and the tissue region located between two flow channels with the same axial extent (3 mm in this case). Twenty A-line segments from the each region were used.

2. Contrast Ratio: As can be seen from results given below, the dynamic range (in decibels) of images from quadratic components is approximately twice the dynamic range of standard B-mode and SH images. In order to account for image perception on standard 8-bit display, all images are represented with their full dynamic range mapped to 256 gray levels. That is,

$$I = \left(\frac{A - A_{\min}}{A_{\max} - A_{\min}}\right) \times 255. \tag{16}$$

where A is the log magnitude pixel values, given by

$$A = 20\log_{10}\left\{\left|\left[\frac{\mathcal{H}(x)}{x_{\text{ref}}}\right]\right|\right\}. \tag{17}$$

where $\mathcal{H}(x)$ denotes the Hilbert transform of data vector, x, and $x_{\text{ref}}(> 0)$ is some constant (typically maximum amplitude). The data vector is the digitized RF for standard B-mode and the output of the harmonic or the quadratic filter for the harmonic and quadratic images, respectively.

$A_{\min}$ and $A_{\max}$ are minimum and maximum values, respectively. Both $A_{\min}$ and $A_{\max}$ are carefully computed so that histograms of images cover 256 gray levels without saturation. This was achieved by finding the average of the minima (maxima) of all image lines after median filtering. This was done to ensure that the display range is not set by extreme values of $A_{\min}$ or $A_{\max}$.

From gray-level images, the contrast ratio (CR) [15] used as the contrast measurement between any two regions is given by

$$\text{CR} = \frac{|I_1 - I_2|}{\sqrt{\sigma_1^2 + \sigma_2^2}}. \tag{18}$$

where I_1 and I_2 are the average of gray levels, and σ_1 and σ_2 are the corresponding standard deviations in the first region and the second region, respectively.

3. Histogram and Receiver Operating Characteristic Analysis: In the imaging results shown below, we evaluate the CTR and CR based on regions in the image representative of the UCA and tissue regions with the same number of pixels and at the same depth. When the number of pixels in these regions is sufficiently high to produce meaningful statistics, histograms of the pixel data are produced to demonstrate these statistics. In addition, receiver operating characteristics (ROC) analysis [16] is performed as a simple method for classification of the different regions. In addition, when additional regions can be identified (e.g., low-scattering regions) in any image, the CR between tissue and such regions is also evaluated. Please note that the ROC curves are included in this paper to further quantify the degree of overlap between different histograms from tissue, contrast, and low-scattering regions.

D. *Resolution Measurements*

We used correlation lengths calculated from the 2D autocorrelation of echoes in tissue regions as described in [17] to measure spatial resolution. Intensity images are scan converted and uniform speckle regions were identified to compute the average speckle correlation cell size

$$S_C = \int_{-X}^{X}\int_{-Y}^{Y}\frac{C_I(x,y)}{C_I(0,0)}\,dx\,dy. \tag{19}$$

where $C_I(x,y)$ is the 2D correlation function of the intensity autocovariance function, and X and Y are taken to be sufficiently large to allow the magnitude of the autocovariance to drop to negligible levels. The vertical and horizontal correlation cell sizes, representing the axial and lateral resolution, respectively, were used to compare spatial resolution for the three imaging techniques.

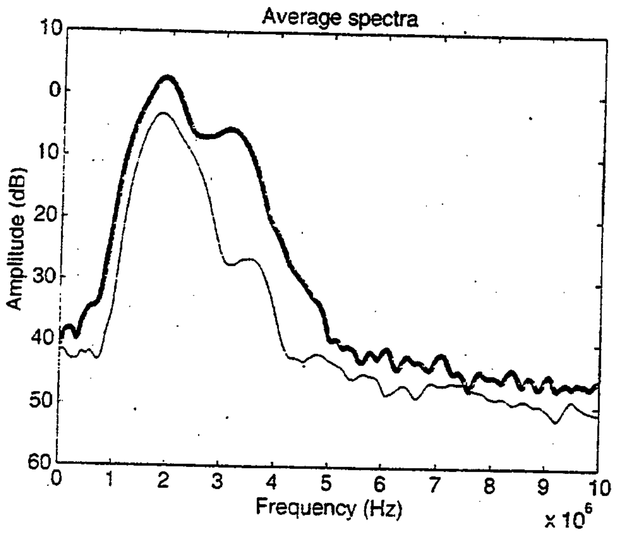

Fig. 5. Average spectra from the contrast (thick) and tissue (thin) regions of the L-shaped phantom.

IV. Results

A. L-Shaped Phantom

Fig. 5 shows the average spectra of typical echoes from the contrast and tissue regions of the L-shaped phantom. The average spectra were calculated by averaging windowed periodogram of every echo line in regions described in Section III-C.1. These spectra suggest that echoes from the contrast region have broader bandwidth compared to the echoes from tissuelike region. As mentioned in Section II-D, this suggests that the best linear filter for contrast enhancement may not be the standard SH filter. Rather, a general BPF with center frequency and relative bandwidth designed to maximize the CTR may be sought. Based on this approach, we have designed a zero-phase BPF with center frequency of 3.2 MHz and relative bandwidth of 30% to demonstrate the performance of linear postbeamforming harmonic imaging. The quadratic filter was derived from echoes from the tissue region according to the algorithm described in Section II-C (with $P = Q = 10$ in Fig. 2). Panels (a), (b), and (c) of Fig. 6 show images obtained using standard B-mode, linear BPF, and quadratic imaging methods, respectively. Due to differences in dynamic ranges for the three methods, each image is displayed with its full dynamic range as can be seen from the decibel-level scale bars shown in accordance with (16). Fig. 6(d) shows four rectangular regions used for characterization of the imaging results. Regions A_1 and A_2 are representative of tissue and contrast echoes, respectively. Regions B_1 and B_2 are representative of tissue and echo-free region, respectively. These regions are used for CTR calculations as well as evaluating histograms of the reconstructed images. Due to the structure of the target, regions B_1 and B_2 could not be placed at the same depth in the image. Nevertheless, region B_1 is representative of tissue response and provides a valid baseline for comparison of contrast with the echo-free region, B_2. The standard B-mode image (Fig. 6(a)) was obtained from the digitized RF echo data and displayed with a dynamic range of 60 dB. The structure of the L-shaped phantom can be recognized with low contrast between the UCA and the tissue-mimicking regions. The strong specular reflection at the top of the UCA region is due to a boundary layer formed by the agent at the interface with the tissue-mimicking medium. A careful examination of the image reveals a higher level of contrast between the two regions at close range. A CTR value of 6.69 dB was computed based on echo signals from regions A_2 and A_1 (Fig. 6(d)).

The linear harmonic BPF image shown in Fig. 6(b) was produced by filtering the RF data with bandpass filter centered around the second harmonic (3.2 MHz) with a fractional bandwidth of 30%. The center frequency and the fractional bandwidth of the harmonic filter were chosen to optimize the CTR value for regions A_1 and A_2 in Fig. 6(d). The CTR value for the harmonic image (18.2 dB) is consistent with the perceived enhancement clearly visible in the image. One can also observe the loss of the specular reflections at the top right and bottom left of the harmonic image. This is typical since these echoes have significant low frequency components. As expected, the speckle in the tissue region appears finer than that of the standard B-mode.

The quadratic image obtained using the algorithm described in Section II-C is shown in Fig. 6(c). The CTR for this image is 21.3 dB indicating contrast enhancement over both standard B-mode and harmonic images. One important feature of the quadratic image is the increased dynamic range compared with B-mode and harmonic images. This increased dynamic range results in contrast enhancement without loss in image features, such as specular reflections, which may be of diagnostic value in some cases.

Another interesting comparison among the three image results shown in Fig. 6(a)–(c) is the echo-free region visible at the right edge of the scan. One can see that contrast between tissue and this region in the quadratic image is superior to that from the B-mode image, whereas this contrast in the harmonic image is the lowest. This result is significant because echo signals from this region are largely artifacts (due to beamforming and/or reverberations). Quantitative measures of this contrast enhancement between the tissue and echo-free regions are given below.

To further illustrate the imaging results given in Fig. 6, vertical and horizontal lines through images are plotted in Fig. 7. Axial lines from the three imaging techniques through the UCA region are shown in Fig. 7(a). One can see that the specular reflector is all but eliminated in the harmonic image, while it remains visible for the other two methods. Further, the axial line from the quadratic image shows no apparent loss in the axial resolution at the specular reflection location. Lateral lines at the 90-mm depth from the three imaging techniques are shown in Fig. 7(b). These lateral lines pass through the UCA, tissue, and the

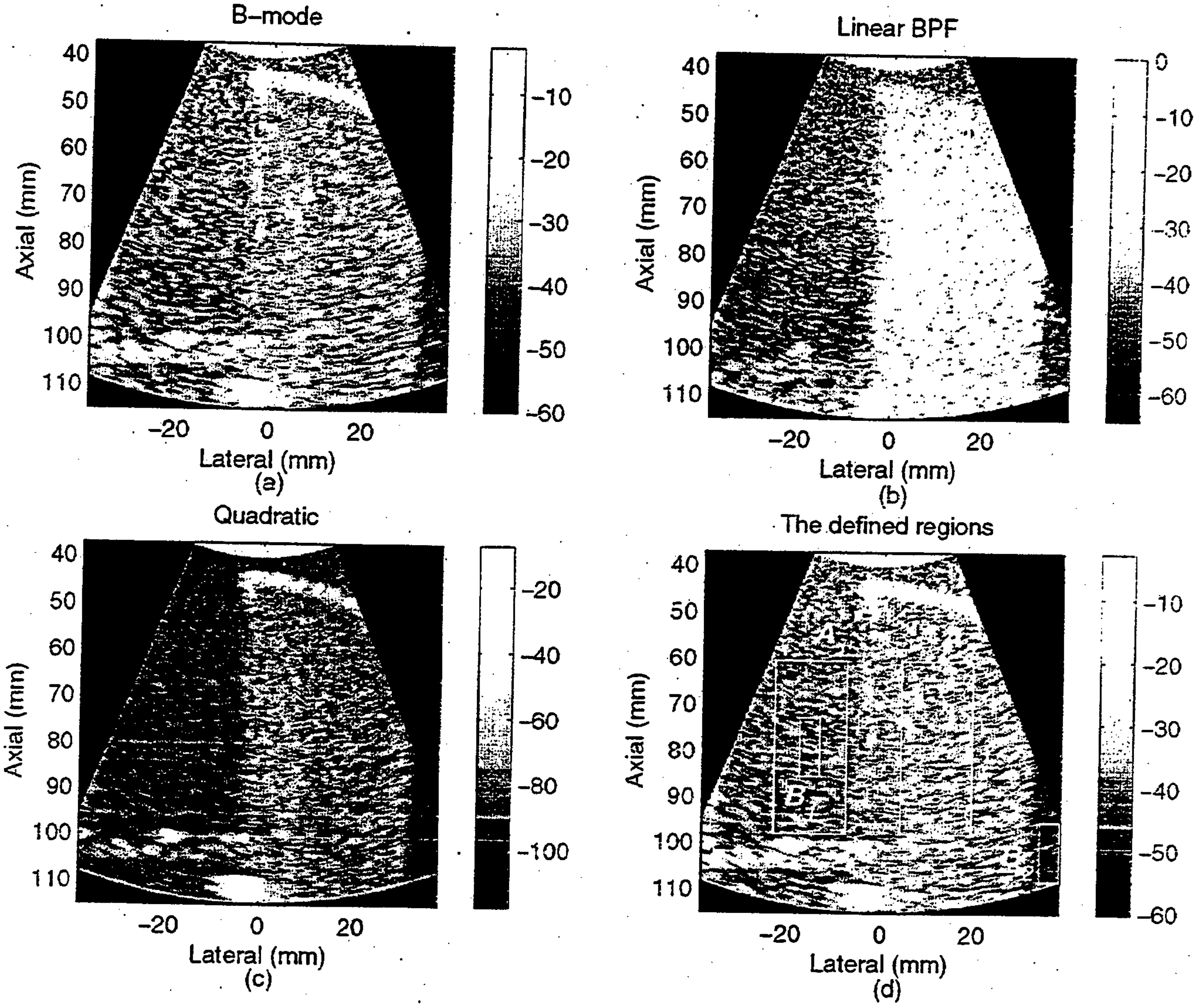

Fig. 6. Images of the beaker containing the tissue-mimicking L-shaped phantom surrounded by the UCA from three imaging techniques. (a) Standard B-mode. (b) Linear harmonic BPF. (c) Quadratic. (d) Boxes indicate regions for CTR and histogram calculations.

echo-free regions. One can see the contrast enhancement from the lateral line of the harmonic image compared with the lateral line of the standard B-mode image. Most significantly, however, one can see that the quadratic image provides the maximum separation between the three regions without apparent loss of lateral resolution. This was confirmed by computing the correlation cell size in the scan-converted intensity images according to (19) [17] from the three imaging methods in the tissue region (59 to 73 mm axial and −20 to −14 mm lateral in Fig. 6). These values are reported in Table I.

B. Flow Channel Phantom

Fig. 8 shows the average spectra of typical echoes from the contrast and tissue regions of the flow phantom described in Section III-B. The average spectra are calculated by averaging windowed periodogram of every echo line in regions described in Section III-C.1. As with the L-shaped phantom result, the echoes from the UCA region exhibit broader bandwidth than those from tissue region. The standard B-mode image of the flow phantom consisting of the UCA and cellulose in flow channels was acquired using the experimental setup described in Section III-B. The image is shown in Fig. 9(a). One can see the backscattered enhancement due to the UCA in the 6-mm flow channel (55- to 61-mm axial and −6 to 0 mm lateral) compared with the surrounding tissue with CTR 9.8 dB. The CTR was calculated based on echo signals from the 6-mm flow channel excluding the specular reflectors (Box C_1) and echoes from tissue at the same depth (Box C_2). On the other hand, the echoes from the cellulose in the 8-mm flow channel (53 to 61 mm axial and 17 to 25 mm lateral) are weaker than those from the surrounding tissue. A linear scatterer-to-tissue ratio (LTR) was calculated based on echo signals from the 8-mm flow channel

TABLE I

CR, CTR, AND CORRELATION CELL SIZE VALUES FOR THE L-SHAPED IMAGING TARGET. THE CTR VALUES ARE GIVEN AS MEAN IN DECIBELS WITH STANDARD DEVIATION IN PARENTHESES.

Imaging method	UCA/T-Mimic	T-Mimic/E-F	CTR	S_z	S_x
B-mode	0.94	1.51	6.65 (1.3)	1.2	2.3
SH	2.56	1.12	18.2 (1.6)	1.0	1.6
Quadratic	2.16	1.66	21.3 (1.9)	0.42	0.8

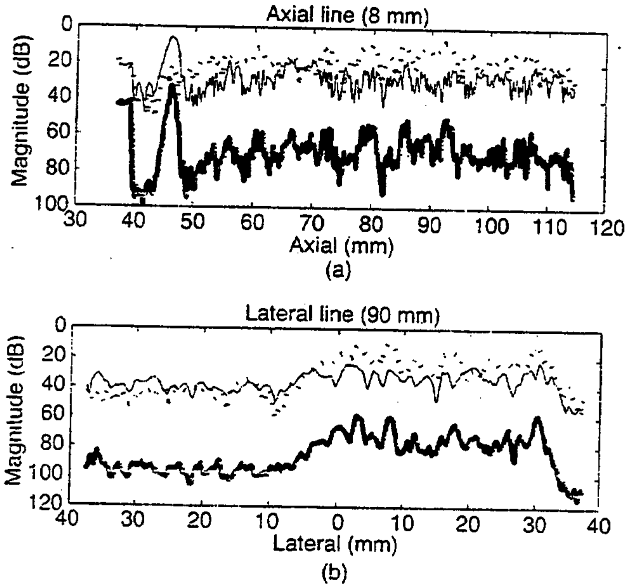

Fig. 7. Lines through images in Fig. 6 from three imaging techniques. Thin: B-mode. Dash: Harmonic. Thick: Quadratic. (Top) Axial lines through the UCA region. (Bottom) Lateral lines (at depth 90 mm) through the tissue-mimicking, UCA, and echo-free regions.

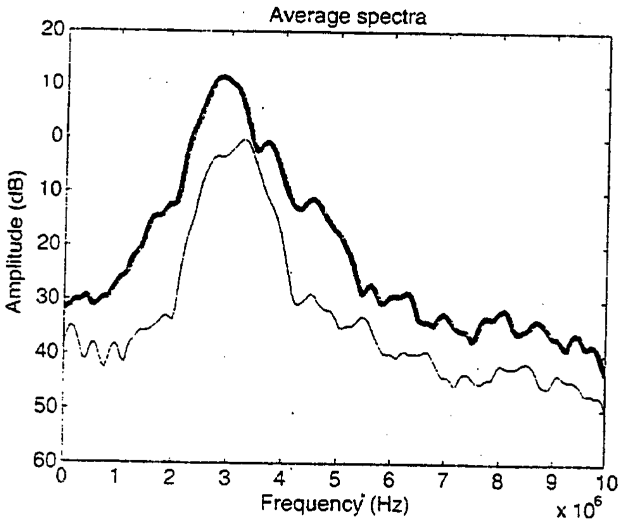

Fig. 8. Average spectra from the contrast (thick) and tissue (thin) regions of the flow phantom.

(Box C_3) and echoes from tissue at the same depth (Box C_2). The LTR was −8.8 dB, calculated based on (11) for 8-mm channel.

The harmonic image shown in Fig. 9(b) was produced by filtering the RF data with bandpass filter centered around 4.8 MHz with a fractional bandwidth of 30%. The center frequency and the fractional bandwidth of the harmonic filter were chosen to optimize the CTR value using the method described in Section II-D for the UCA and tissue regions shown in Fig. 9(d). The CTR value for the harmonic image is 15 dB, which is consistent with the perceived enhancement clearly visible in the displayed image. It is interesting to note the loss of the specular reflections from the contrast flow channel but not from the linear scatterer channel. It is also interesting to note that the speckle in the tissue region is finer than that of the standard B-mode. This indicates that the optimization of the harmonic filter resulted in a larger fractional bandwidth than that of the fundamental component. The LTR for the harmonic component is now −7.6 dB. That is, the harmonic image does not preserve the low-scattering region as it improves the contrast between the UCA and tissue regions.

Fig. 9(c) shows the quadratic image obtained using the algorithm described in Section II-C (with $P = Q = 12$ in Fig. 2). Compared with the standard B-mode, the enhanced visualization of the UCA in the small flow channel surrounded by the tissue can be seen. This enhanced visualization is also consistent with the higher CTR (22.2 dB). In addition, one can see the reduction in the echogenicity of the cellulose in the 8-mm flow channel. This is also reflected in the value of LTR (−15.4 dB) computed for this channel. This result demonstrates the ability of the quadratic filter to separate the tissue from both the UCA and the low-scattering cellulose region simultaneously. We can also see the preservation of specular reflections from both the UCA and cellulose flow channels. This can be seen more quantitatively in Fig. 10, which shows the decibel values for axial and lateral lines through images in Fig. 9. Axial lines through the center of the cellulose and the UCA flow channels are shown in Fig. 10(a) and Fig. 10(b), respectively. Lateral lines through the center of both the cellulose and the UCA flow channels are shown in Fig. 10(c). One can see the contrast enhancement in different media (i.e., the UCA, the cellulose, and the tissue) from the quadratic image without loss in spatial resolution. In particular, for the B-mode image, the signal from the contrast channel is 13 dB above the tissue level and 30 dB above the cellulose channel. On the other hand, for the

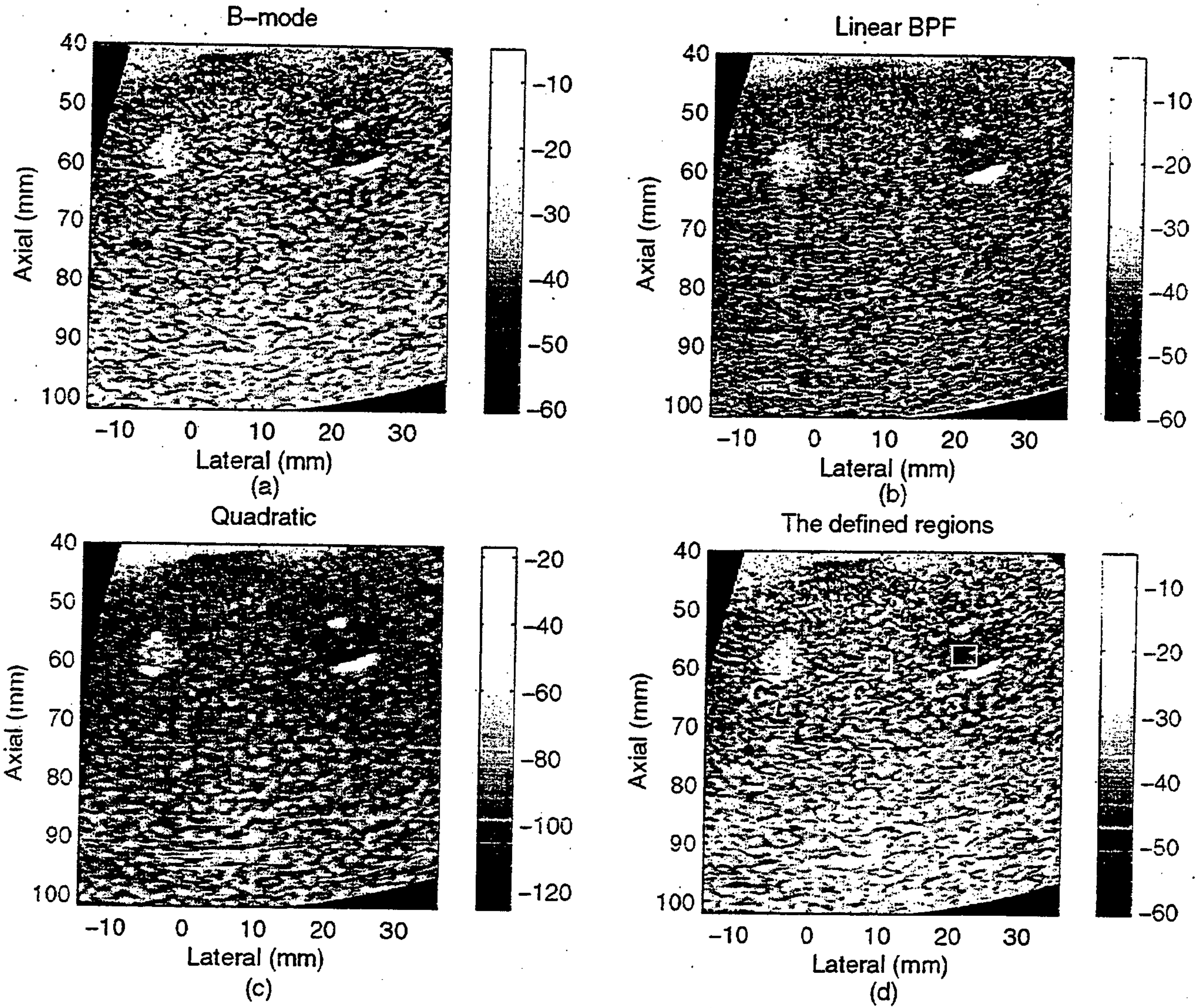

Fig. 9. Images of the flow phantom using (a) Standard B-mode, (b) Harmonic, (c) Quadratic, (d) Boxes C_1, C_2, and C_3 indicate regions for CTR and CR calculations. Note the hyperechoic region from the UCA in the 6-mm flow channel (55 mm to 61 mm axial and −6 mm to 0 lateral) and the hypoechoic region from the cellulose (53 mm to 61 mm axial and 17 mm to 25 mm lateral).

quadratic image, the signal from the contrast channel is 30 dB higher than tissue and 67 dB higher than the cellulose channel. Finally, examination of the strong specular reflections along the axial lines shown in Fig. 10 suggests that the quadratic filter preserves the resolution of the system. This was confirmed by computing the correlation cell size in the scan-converted intensity images according to (19) [17] from the three imaging methods in the tissue region (52 to 65 mm axial and 4 to 17 lateral in Fig. 7). These values are reported in Table II.

C. Classification Results

To give the reader a quantitative idea of the ability of the three different imaging methods to separate the different regions in the imaging targets, we use histograms from representative areas of these regions. For example, for the tissue-mimicking L-shaped phantom surrounded by the UCA in the beaker, regions from different media are defined in Fig. 6(d) as follows: the region A1 and A2 (the tissue and UCA regions, respectively) and the region B1 and B2 (the tissue and echo-free regions, respectively). After images from three different imaging techniques are scan converted and represented with 256 levels of gray covering their full dynamic range, the histogram of each region is determined and shown in Fig. 11. Histograms from regions A1 and A2 are shown in Fig. 11 (left-hand side). One can see the degree of overlap between the histograms is highest for the standard B-mode image. On the other hand, the corresponding histograms are well separated for the harmonic and quadratic images. This is consistent with the increased level of contrast perceived from direct visualization of the images in Fig. 6. Histograms produced from regions B1 and B2 are shown in

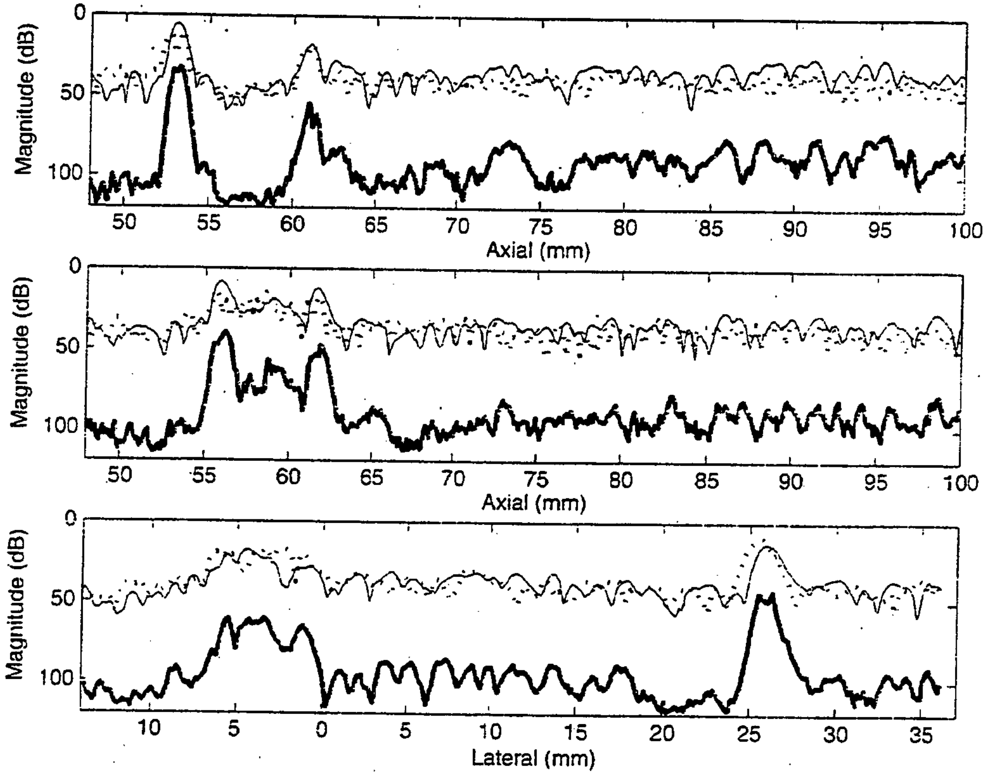

Fig. 10. Lines through the standard B-mode (thin), harmonic (dashed), and the quadratic (thick) from images shown in Fig. 9 (Top) Axial lines through the center of the cellulose flow channel. (Middle) Axial lines through the center of the UCA flow channel. (Bottom) Lateral lines through the center of both two flow channels.

TABLE II

CR, CTR, AND CORRELATION CELL SIZE VALUES FOR THE FLOW CHANNEL TARGET. THE CTR VALUES ARE GIVEN IN DECIBELS

Imaging method	UCA/Tissue	Tissue/Cellulose	CTR	S_z	S_x
B-mode	1.57	1.35	9.8	1.0	1.2
SH	2.12	1.21	15.0	0.6	0.9
Quadratic	2 46	1.65	22.2	0.9	1.1

Fig. 11 (right-hand side). Gray-level histograms of regions B1 and B2 produced from harmonic image has higher degree of overlap than those from the standard B-mode and the quadratic images. This is further quantified by ROC curves [16] obtained from histograms of region A1 (Tissue) and A2 (UCA) and region B1 (tissue) and B2 (echo-free) are shown in Fig. 12(a) and Fig. 12(b), respectively. As can be seen in Fig. 12(a), the A_z values between region A1 and A2 from the standard B-mode, harmonic and quadratic images are 0.8269, 0.9936, and 0.9876, respectively. These values demonstrate improved classification performance between region A1 and region A2 from harmonic and quadratic images over the standard B-mode image. However, as shown in Fig. 12(b), the A_z value of the quadratic image (0.9535) presents the best classification performance of tissue and echo-free regions among three imaging techniques, while the classification performance from the harmonic image (A_z = 0.8724) is inferior to that from the standard B-mode image (A_z = 0.9302). These measurements show that the quadratic image provides improved separation of the UCA from the tissue mimic comparable with SH performance. At the same time, significant improvement in separation between tissue mimic and echo-free regions is achievable in the quadratic image over both the standard B-mode and SH images.

Contrast ratios determined from corresponding gray scale images in Fig. 6 are shown in Table I. For contrast comparison between the UCA and tissue regions, CRs obtained from regions A1 and A2 demonstrate the contrast enhancement of the harmonic (2.56) and the quadratic (2.16) images over the standard B-mode image (0.94). On the other hand, one can see that the CR between tissue and echo-free regions of the harmonic image (1.12) is inferior to that of the standard B-mode image (1.51). However, the quadratic image gives the maximal CR (1.66). These CR values agree with both the visualization of images shown

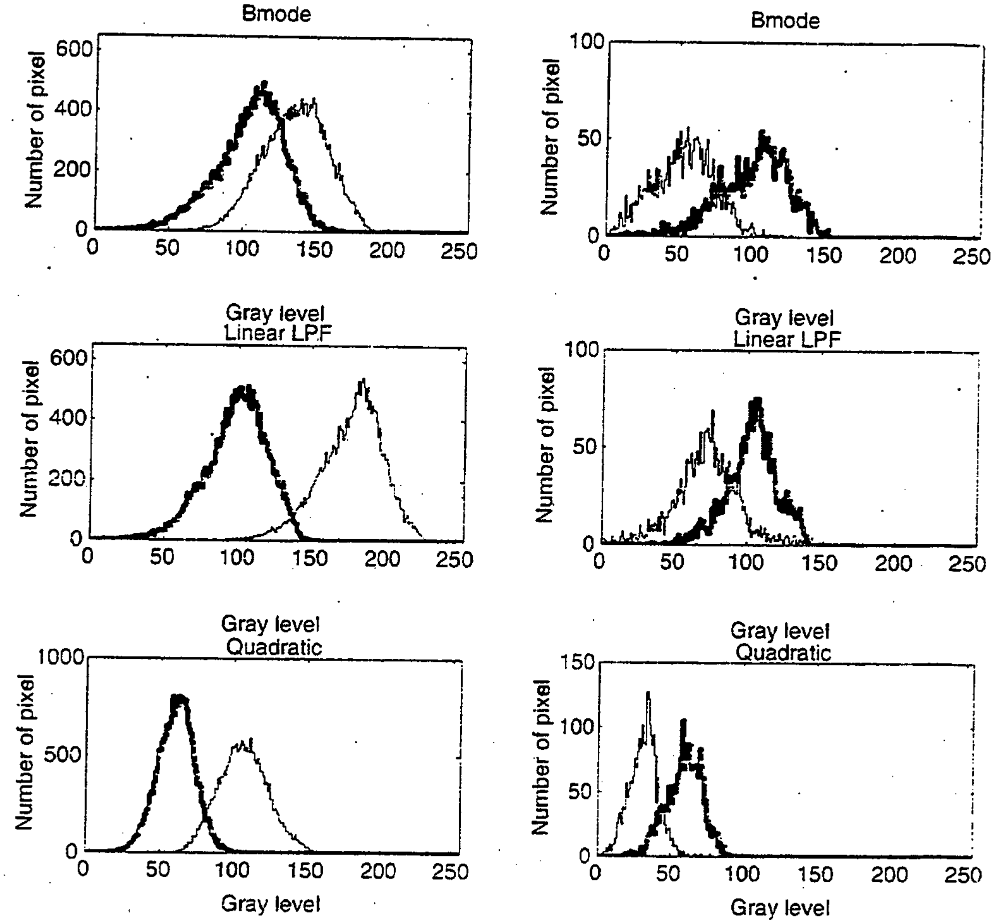

Fig. 11 Gray-level histograms produced from images shown in Fig. 6. Top: B-mode. Middle: Harmonic. Bottom: Quadratic. Histograms on the left-hand side are produced from region A1 and A2 Thick: Region A1 (Tissue). Thin: Region A2 (Contrast) Histograms on the right-hand side are produced from region B1 and B2. Thick: Region B1 (Tissue). Thin: Region B2 (Air).

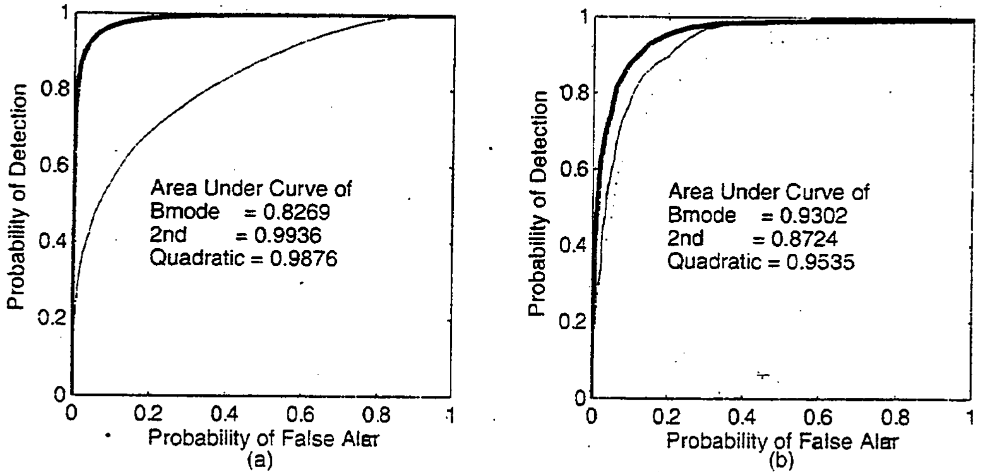

(a) (b)

Fig. 12 The ROC curves produced from gray-level histograms in Fig. 11 of three imaging techniques. Thick: B-mode. Dash: Harmonic Thin: Quadratic. The ROC curve obtained from the UCA and tissue regions is shown on the left-hand side. The ROC curve obtained from the echo-free and tissue regions is shown on the right-hand side.

in Fig. 6 and the degree of overlap between the histograms shown in Fig. 11. These results have demonstrated that the quadratic image provides the perceived contrast enhancement not only between the UCA and tissue regions but also between the tissue and the echo-free regions. We note here that similar analysis was performed for the flow channel data and that the results are in full agreement with the results shown in this section. The CR, CTR, and correlation cell size values for both the L-shaped and flow phantoms are summarized in Tables 1 and 2.

Similarly, images of the UCA and cellulose flow channels in the flow phantom as shown in Fig. 9 are scaled into 8-bit gray-level images. Gray-level histograms between the UCA and tissue regions and between the cellulose and tissue regions are produced and the corresponding ROC curves are determined. Although the number of data from each region is quite small for meaningful statistical analysis, results from both CRs and A_z show tendency that the quadratic image enhances the contrast and provides better classification performance compared with the standard B-mode image. Table II gives the CR values resulting from the flow channel experiment.

V. DISCUSSION

We have introduced a nonlinear postbeamforming filtering algorithm for ultrasonic pulse-echo imaging based on the Volterra filter model. The main goal of this paper was to introduce the mathematical basis for deriving the filter coefficients from standard beamformed RF data obtained by commercial scanners. In addition, we have presented imaging results from two laboratory contrast targets to illustrate the nature of the gray scale images obtained with the quadratic component compared with standard echo signals and harmonic images. Images from the quadratic components were obtained by applying a single filter derived from echoes from the contrast region. We have decided to do this to demonstrate that the method is quite robust in the sense that the derived filter is applied throughout the image to produce images free of artificial inhomogeneity. This is a desirable method from the implementation point of view, especially for real-time implementation.

For a fair comparison, all images presented in this paper were normalized to their full dynamic range and displayed using 256 levels of gray. Classification results based on histogram characterization of contrast and tissue regions show that the quadratic images produce nearly twofold increase in CR values (compared with standard echo images) without loss of image features (compared to harmonic images). Classifying the tissue and echo-free regions demonstrated the improved performance with respect to harmonic imaging. This is probably due the vulnerability of harmonic images to noise and beamforming artifacts, especially when the sidelobes of the transmit beam are in contrast regions.

Even though we have focused on the comparison between gray-scale images, there are some interesting properties of the quadratic signal components that may reveal important information on the nature of the objects producing the echo signals. For example, the frequency component at f in the quadratic signal component is a result of all frequency components f_1 and f_2 from the echo signal such that $f_1 + f_2 = f$, weighted by $H_Q(f_1, f_2)$. This frequency coupling results in quadratic signal components with high SNR values due to rejection of additive noise. An interesting question is whether the quadratic components are more directly related to the composition of the echoes in terms of coherent and diffuse scattering. This may be quite significant in improving the robustness of motion tracking and displacement estimation algorithms.

In this paper, the filter is designed based on nonlinear echoes from the tissue-like medium. However, the filter does not distinguish between nonlinearities from UCA and those from tissue. The contrast enhancement is mainly due to the higher level of quadratic component (relative to the RF signal level) in the contrast regions. For example, in the L-shaped phantom, on average, the quadratic signal is 30 dB and 50 dB below the RF in the contrast and tissue regions, respectively. It is interesting to note that, for this target, the quadratic component from the magnetic bead at the bottom of the image is only 3 dB below the RF signal. This suggests that the quadratic filter does not completely reject quadratic echoes from specular reflectors, even though it may still discriminate against them. Therefore, for applications in which the quadratic components from the contrast agents are weak or comparable to tissue components, a method for separating the two types of nonlinearity is needed. There are several possible approaches to the filter design problem so that better separation between nonlinear echoes from UCA and tissue:

- Adaptive implementation of the SVF based on fast recursive LS approach [12]. This will allow for the optimization of filter coefficients based on the local level of nonlinearity.
- Higher order filters (e.g., cubic) that may be more sensitive to UCA nonlinearity than tissue nonlinearity. This is due to the observation that, under normal imaging conditions, tissue nonlinearity is at most quadratic.
- Synthesis of pulse sequences to excite contrast microbubbles to maximize their nonlinear response. This is motivated by the recent trend in contrast-agent imaging, which calls for the use of super low values of MI. The identified quadratic kernel of the SVF can be used for the design of these waveforms

We have chosen to compare quadratic images with images obtained using linear harmonic filters rather than second harmonic filters. This was based on the observation that the spectra of echoes from contrast regions are typically broader than those from tissue regions as can be seen from Figs. 5 and 8. The application of a strict SH filter based on the bandwidth from tissue component typically produce inferior results when UCA regions are present in the imaging field. To illustrate this point, Fig. 13 shows

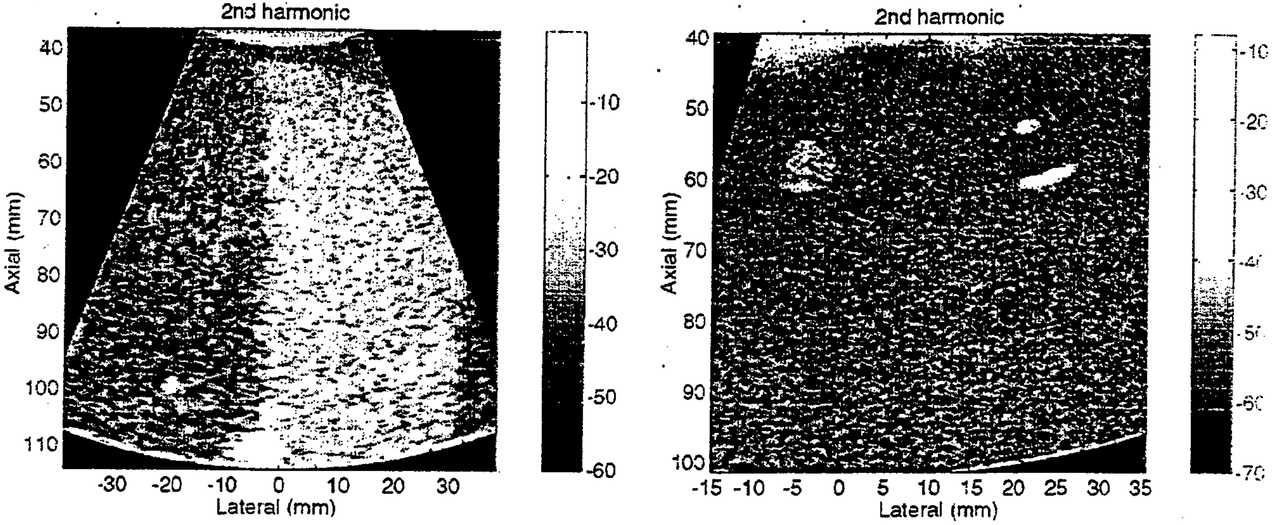

Fig. 13. LHS: The image of L-shaped phantom produced using BPF centered at 4 MHz with fractional bandwidth 25%. RHS: The image of flow channel phantom produced using BPF centered at 6 MHz with fractional bandwidth 25%.

SH images of both the L-shaped and flow phantoms based on the spectra from tissue regions. These images are visibly inferior to those obtained using the linear harmonic approach described in Section II-D. We note that quantitative analysis of these images confirms the inferiority of the SH images shown.

The filters used for extracting the quadratic components for the two data sets were of orders 10 and 12 for the L-shaped phantom and the flow-channel phantom, respectively. In deriving the filters, we have assumed that $h_Q(j,k) = h_Q(k,j)$, which implies that the filters can be implemented with 65 and 90 independent coefficients, respectively. On the other hand, the linear bandpass filter had 77 coefficients. This number is effectively doubled by the zero-phase implementation described in Section II-D. While it is not our objective to compare the computational efficiency of the quadratic filters with the linear filter, we note that the requirements of the quadratic filters will not present a severe problem for real-time implementation on modern ultrasound scanners. We also note that efficient software and hardware implementations of the Volterra filter have been extensively studied in recent literature [19].

Finally, even though the two imaging targets in this paper contain UCA regions, quadratic images can be used in "native quadratic" form, in much the same way as SH images. The enhancement of the contrast between the tissue mimic and the low scattering regions in both targets offer an illustration of the nature of quadratic images in native mode. We are currently investigating speckle reduction in quadratic images (some speckle reduction can be observed in the tissue mimic in quadratic images from both phantoms). This is the subject of a future report.

VI. CONCLUSIONS

A nonlinear postbeamforming filter based on the Volterra model was introduced in this paper. The quadratic component from the SVF signal separation model was shown to produce images with high contrast and high dynamic range without loss of axial or lateral resolution. This was confirmed by estimating the correlation cell size based on [17] for the quadratic images and comparing with those for B-mode and Harmonic images (Tables I and II). The improvement in contrast was confirmed by quantitative measures, both on the RF data and the log-compressed image data after scan conversion. Furthermore, the quadratic images were also shown to preserve the low-scattering targets while improving the UCA to tissue contrast. This was demonstrated by the computed CR values (Tables I and II) and the A_z values from the ROC curves shown in Fig. 12.

ACKNOWLEDGMENTS

We are indebted to Prof. Franco Bertora from Esaote for his help and support on all aspects of this research. We are also grateful for Dr. Paolo Pellegretti from Esaote for help with data acquisition and valuable suggestions. The RF data for the L-shaped phantom was provided by Dr Marcel Arditi from Bracco Research. We are also thankful for Hui Yao for helping with the flow channel experimental setup.

REFERENCES

[1] J. Ophir and K. J. Parker, "Contrast agent in diagnostic ultrasound," *Ultrasound Med. Biol.*, vol. 15, no. 4, pp. 319-333, Nov. 1989.

[2] J. D. Kasprzak, B. Paelinck, F. J. Ten Cate, W. B. Vletter, N. de Jong, D. Poldermans, A. Elhendy, A. Bouakaz, and J. R. Roelandt, "Comparison of native and contrast-enhanced harmonic echocardiography for visualization of left ventricular endocardial border," *Amer. J. Cardiol.*, vol. 83, no. 2, pp. 211–217, 1999.

[3] S. Kaul and R. Jayaweera, "Coronary and myocardium blood volumes: Noninvasive tools to assess the coronary microcirculation," *Circulation*, vol. 96, pp. 719–724, 1997. **[AU: Need issue number or month of issue.]**.

[4] P. J. A. Frinking, E. Cespedes, J. Kirkhorn, H. Torp, and N. de Jong, "A new contrast ultrasound imaging approach based on the combination of multiple imaging pulses and a separate release burst," *IEEE Trans. Ultrason., Ferroelect., Freq. Contr.*, vol. 48, no. 3, pp. 643–651, May 2001.

[5] P. J. A. Frinking, A. Bouakaz, J. Kirkhorn, F. J. Ten Cate, and N. de Jong, "Ultrasound contrast imaging: Current and new potential methods," *Ultrasound Med. Biol.*, vol. 26, pp. 965–975, 2000. **[AU: Need issue number or month of issue.]**.

[6] N. de Jong, P. J. A. Frinking, A. Bouakaz, and F. J. Ten Cate, "Detection procedures of ultrasound contrast agents," *Ultrasonics*, vol. 38, pp. 87–92, 2000. **[AU: Need issue number or month of issue.]**.

[7] D. H. Simpson, C. T. Chin, and P. N. Burns, "Pulse inversion Doppler: A new method for detecting nonlinear echoes from microbubble contrast agent," *IEEE Trans. Ultrason., Ferroelect., Freq. Contr.*, vol. 46, no. 2, pp. 372–382, Mar. 1999.

[8] D. H. Simpson and C. T. Chin, "Perfusion imaging with pulse inversion Doppler and microbubble contrast agents: In vivo studies of the myocardium," in *Proc. IEEE Ultrason. Symp.*, 1998, vol. 2, pp. 1784–1786.

[9] H. Yao, P. Phukpattaranont, and E. S. Ebbini, "Postbeamforming second-order volterra filter for nonlinear pulse-echo imaging," in *ICASSP*, vol. 2, 2002, pp. 1133–1136. **[AU: Spell out ICASSP]**.

[10] K. I. Kim and E. J. Powers, "A digital method of modeling quadratically nonlinear systems with a general random input," *IEEE Trans. Acoust. Speech Signal Processing*, vol. ASSP-36, no. 11, pp. 1758–1769, Nov. 1988.

[11] T. Koh and E. J. Powers, "Second-order volterra filtering and its application to nonlinear system identification," *IEEE Trans. Acoust. Speech Signal Processing*, vol. ASSP-33, no. 6, pp. 1445–1455, Dec. 1985.

[12] K. Kim, S. B. Kim, E. J. Powers, R. W. Miksad, and F. J. Fischer, "Adaptive second-order volterra filtering and its application to second-order drift phenomena," *IEEE J. Oceanic Eng.*, vol. 19, no. 2, pp. 183–192, Apr. 1994.

[13] G. H. Golub and C. F. Van Loan, *Matrix Computations. 2nd ed.* Baltimore, MD: Johns Hopkins Univ. Press, 1989. **[AU: Need inclusive pages.]**.

[14] J. Shen and E. S. Ebbini, "A new coded excitation ultrasound imaging system: Part 1—Basic principles," *IEEE Trans. Ultrason., Ferroelect., Freq. Contr.*, vol. 43, no. 2, pp. 919–928, 1996.

[15] W. K. Pratt, *Digital Image Processing.* Wiley-Interscience, 1978. **[AU: Need publisher location, inclusive pages.]**.

[16] C. E. Metz, "ROC methodology in radiologic imaging," *Investigative Radiol.*, vol. 21, no. 9, pp. 720–733, 1986.

[17] R. F. Wagner, M. F. Insana, and S. W. Smith, "Fundamental correlation lengths of coherent speckle in medical ultrasonic images," *IEEE Trans. Ultrason., Ferroelect., Freq. Contr.*, vol. 35, no. 1, pp. 34–44, Jan. 1988.

[18] S. K. Mitra, *Digital Signal Processing: A Computer-Based Approach. 2nd ed.* New York: McGraw-Hill, 2001. **[AU: Need inclusive pages.]**,

[19] V. J. Mathews and G. Sicuranza, *Polynomial Signal Processing.* New York: Wiley, 2000. **[AU: Need inclusive pages.]**.

Pornchai Phukpattaranont was born in Songkla, Thailand, in 1970. He received his B. Eng. and M. Eng. degrees in Electrical Engineering from Prince of Songkla University in 1993 and 1997, respectively. His M. Eng. thesis was on the sequential electrical stimulator for dysphagia patients. He is currently working toward his Ph.D. degree in Electrical and Computer Engineering at the University of Minnesota. His research interests are ultrasound contrast imaging and ultrasound signal processing.

Emad S. Ebbini (S'84–M'85–S'86–M'89) received his B.Sc. in EE/communications in 1985 from the University of Jordan and the M.S. and Ph.D. degrees in EE from the University of Illinois at Urbana-Champaign in 1990. From 1990 until 1998, he was on the faculty of the EECS department at the University of Michigan, Ann Arbor. Since 1998 he has been with the ECE department at the University of Minnesota. In 1993, he received the NSF Young Investigator Award for his work on new ultrasound phased arrays for imaging and therapy. He was a member of AdCom for the IEEE Ultrasonics, Ferroelectrics, and Frequency Control between 1994 and 1997. In 1996, he was a guest editor for a special issue on therapeutic ultrasound in the *IEEE Transactions on Ultrasonics, Ferroelectrics, and Frequency Control.* He was an associate editor for the same transactions from 1997–2002. He is a member of the standing technical program committee for the IEEE Ultrasonics Symposium and a member of the Board of the International Society for Therapeutic Ultrasound. His research interests are in signal and array processing with applications to biomedical ultrasonics.